The Pennsylvania State University

The Graduate School

Department of Engineering Science and Mechanics

A SELF-CONTAINED, NANO-GAP BIOMOLECULE CAPACITANCE SENSOR SYSTEM WITH NANOFLUIDIC CONTROL

A Dissertation in

Engineering Science and Mechanics

by

Huinan Liang

Submitted in Partial Fulfillment
of the Requirements
for the Degree of

Doctor of Philosophy

December 2008

The dissertation of Huinan Liang was reviewed and approved* by the following:

Stephen J. Fonash
Bayard D. Kunkle Chair Professor of Engineering Science and Mechanics
Dissertation Advisor
Chair of Committee

Osama O. Awadelkarim
Professor of Engineering Science and Mechanics

Digby D. Macdonald
Distinguished Professor of Materials Science and Engineering

Jian Xu
Assistant Professor of Engineering Science and Mechanics

Judith A. Todd
P. B. Breneman Department Head
Head of the Department of Engineering Science and Mechanics

*Signatures are on file in the Graduate School

ABSTRACT

Biomolecule sensing is particularly important for pharmaceutical and medical development. In the past few decades, biomolecular sensors have undergone several generations of development with the advances in biology, chemistry, and fabrication technology. Present-day biomolecular sensors often comprise Micro-Total Analysis Systems (μTAS) with minimization, integration, and intelligence. The final goal is to realize a Lab-on-a-Chip system which integrates fluid control, biomolecule detection, and processing in one single chip. Currently, most of the developed and utilized biomolecular sensors are based on a variety of technologies such as fluorescence probe detection, surface plasmon resonance detection (SPR), ion sensitive field effect transistor detection (ISFET), light addressable potentiometric sensor detection (LAPS), surface acoustic wave detection (SAW), and quartz crystal microbalance detection (QCM), etc.

From the point of view of ease of data acquisition and of simplicity of system integration, the final goal of Lab-on-a-Chip biomolecule sensing seems best achieved by using a direct electrical detection method in future biomolecular sensors. Direct electrical detection methods are advantageous in that no signal conversion is required and, more importantly, because their integration with a fluidic control system is relatively straightforward. Capacitive electrical detection schemes are particularly easily integrated.

In this dissertation, a sub-50 nm capacitor sensing structure integrated with micro- and nano-fluidic flow control component has been constructed. It is based on a full analysis, design, and fabrication approach, which addresses noise, sensitivity, and integration issues. This device is composed of an integrated microfluidic flow control

channel in PDMS and a nanofluidic channel in silicon oxide feeding a nano-gap capacitor sensing structure with gold electrodes. Our integrated analytical system is also capable of selectivity. This can be realized by the immobilization of specific probe and target molecules on the gold electrode surfaces.

The molecule detection capability is based on the electrical capacitance change upon probe and target molecule binding on the gold electrode surfaces (spaced 50 nm) in the nano-gap sensing structure. A result of our nano-gap capacitor sensing structure design and optimization analysis is our being able to reduce background noise from the electrical double layers by using the sub-50 nm gap sensing structure to overlap the electrical double layers. This results in the capacitance from the diffuse layers to increase dramatically, therefore, increase the system sensitivity to capacitance component due to probe and target molecule binding.

The possibility of excellent fluidic flow control through the nano-gap sensing structure for active molecule flow and exchange is accomplished by using a unique integrated nanofluidic flow control component, which consists of the microfluidic flow control channel in PDMS connected with the nanofluidic channel in parallel. This parallel flow control (PFC) configuration uses flow in the microfluidic channel to set up the pressure gradient across the nanofluidic channel. This configuration also facilitates the interfacing between nanofluidic systems and external macro fluidic systems.

We also provide a demonstration of the biomolecule sensing capabilities of our analytical systems. Probe molecules (cysteamine) are first self-assembled on the gold electrodes, and target molecules (quantum dots with carboxyl groups) then are bonded with the probe molecules. Both of binding occurrences are detected by measuring the

capacitance change. We are able to detect about 15% capacitance changes with the amino-carboxyl binding occurrence. Optical fluorescence spectra are also obtained to verify that the quantum dots used in this demonstration actually do attach and cause the corresponding capacitance change. This successful electrical detection of the common amino-carboxyl binding process shows the potential detection applications of our systems for other biomolecules.

TABLE OF CONTENTS

LIST OF FIGURES

LIST OF TABLES

ACKNOWLEDGEMENTS

First and foremost, I would like to thank my advisor, Dr. Stephen J. Fonash for his invaluable guidance and support in my graduate work. I still remembered how desperately I was seeking for a new research group and funding after I obtained my Master in Bioengineering in 2004. It was one of the best decisions I made so far (to a previous extremely introverted person speaking crappy English with strong southeastern Chinese dialect accent) to catch this overwhelming academic authority right after his class at Thomas building in one late “fear and trembling” summer afternoon. And later, with the “flattering” words from one of his previous graduate students, Dr. Yinghui Shan now, it was my honor to be picked into his graduate research group. After working in this group for about four years, what I would like to tell now is that Dr. Fonash is absolutely belonging to the category of advisors who I really like to work with again. He is a true visionary with strong and firm understanding of not only numerous theoretical areas, but also broad technical experimental aspects. And he is always supportive of and motivates his students to work at their own fullest potentials. It was my pleasure to work with Dr. Fonash.

I also would like to thank my committee members, Dr. Osama O. Awadelkarim, Dr. Digby D. Macdonald, and Dr. Jian Xu, for their guidance and insight in this work. The invaluable comments and discussions they provided are always highly appreciated.

I would like to thank numerous friends from whom I “robbed” endless help both in “tedious” graduate research and “frustrated” daily life. You, Dr. Wook Jun Nam, An

Cheng, and colleagues from the windowless graduate student office, deserve my appreciations.

In addition I would like to thank all the staffs at the Penn State University (PSU) National Nanofabrication Infrastructure Network facility and Materials Characterization Laboratory for their intellectual discussion and technical support. And thank also goes to Dr. Nadine Barrie Smith and Eugene Gerber in Department of Bioengineering for technical support.

Finally, no words can express my gratitude adequately to my family, my parents, my siblings, and my dear wife, for their forever support and love in my life.

To God Almighty for the grace to carry on.

Chapter 1

Introduction

The term biomolecular sensor refers to those devices and instruments which are able to sense biologic or chemical signals and transfer these signals into the other favorable types of formats such as electrical or optical signals. These sensors generally consist of two major parts. One is the molecule recognition device which is made of highly sensitive materials designed to detect target molecules. The second part is the signal transformation device which basically includes the generation of electrical, electrochemical or optical signals upon target molecule binding. Further, with the continuous development of novel materials, principles and technologies, especially the emergence of Micro-Electro-Mechanical Systems (MEMS) technology (1970s) and biochip technology (1990s), current biomolecular sensors often comprise Micro-Total Analysis Systems (μTAS) with minimization, integration, and intelligence.

Following this trend toward full systems on a chip, a novel biomolecule sensing technology is proposed, designed, built, and tested in this dissertation. This system has the following claimed advantages: electrical detection allowing high integration level and full signal processing, as needed, with convenient output, high sensitivity based on highly specific molecule recognition technology, high signal-noise ratio based on the use of a specific nano-gap sensing structure, and high compatibility with external macro fluidic systems derived from the presence of a novel micro- and nano-scale fluidic control component.

1.1 Overview of Biomolecular Sensors

Biomolecular sensors have been studied and developed over the decades since the middle of the 20th century. This development can be traced back to the 1940s when scientists found enzyme molecules have the ability to identify specific biomolecules. By using this specificity, Leland C. Clark pioneered in measuring glucose concentration with the famous Clark oxygen electrode [**1**]. The second generation of biomolecular sensors was developed after the discovering and realization of interactant molecular pairings in biological organisms based on structural affinity, such as enzyme-substrate, enzyme-coenzyme, antigen-antibody, biotin-streptavidin, and double strand DNA, etc. In such pairing couples, one component can be fixed and used as the probe, and hence can be used to catch and detect the other component which is identified as the target. Later straightforward electrical detection was initiated and a third generation of biomolecular sensors was developed based on bio-electronic principles. Recently, micro- and nano-fabrication technologies have been used for manufacturing biomolecular sensors inducing a remarkable evolution. At present, biomolecular sensors can be grouped into two major categories: fluorescence labeling sensors and fluorescence-label-free sensors. In the following section, a brief review of current biomolecular sensors development is presented.

1.1.1 Fluorescence Labeling Biomolecular Sensors

Biomolecular sensors based on fluorescence probe detection technology are the most popular and extraordinarily sensitive analytical systems nowadays especially in

biological field [**2**][**3**]. They can provide an immediate visible image (Figure **1-1**) and near real time detection with extremely high throughputs.

Figure **1-1**: Bovine pulmonary artery endothelial cells stained with red, green and cascade blue dyes [**4**].

The detection mechanism is based on the fundamental fluorescence process which typically is a three-stage process that occurs in certain molecules called fluorophores or fluorescent dyes. These molecules can be excited by an external light source (generally UV light) and then will emit fluorescence light with a longer wavelength after a short delay time (of the order of nanosecond) with a small amount of energy loss (Figure **1-2**). A typical absorption and emission spectrum is shown in Figure **1-3** for a specific fluorophore. With a proper set of optical filters, emission light can be separated from the incident light and collected for subsequent investigation.

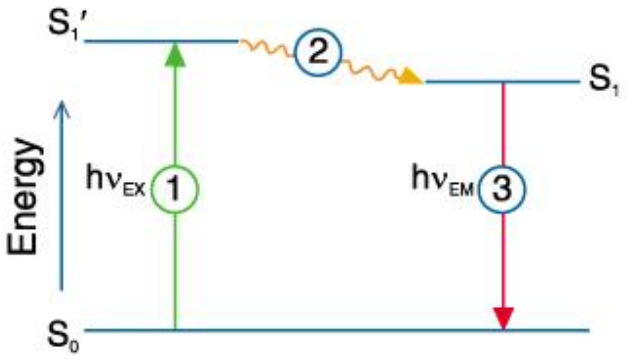

Figure **1-2**: The schematic of fundamental three-stage fluorescence process [**4**].

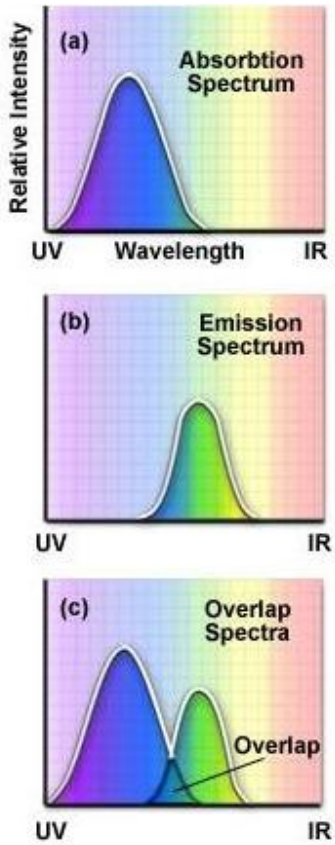

Figure **1-3**: Fluorescence absorption spectrum and emission spectrum [**4**].

By modifying these fluorophore molecules with diverse probe biomolecules, this technology has been widely applied in detecting particular target molecules or components of complex biomolecular assemblies, including live cells, with exquisite sensitivity and selectivity [**5**][**6**]. It has also been proven useful for monitoring cellular events *in vivo* [**7**][**8**].

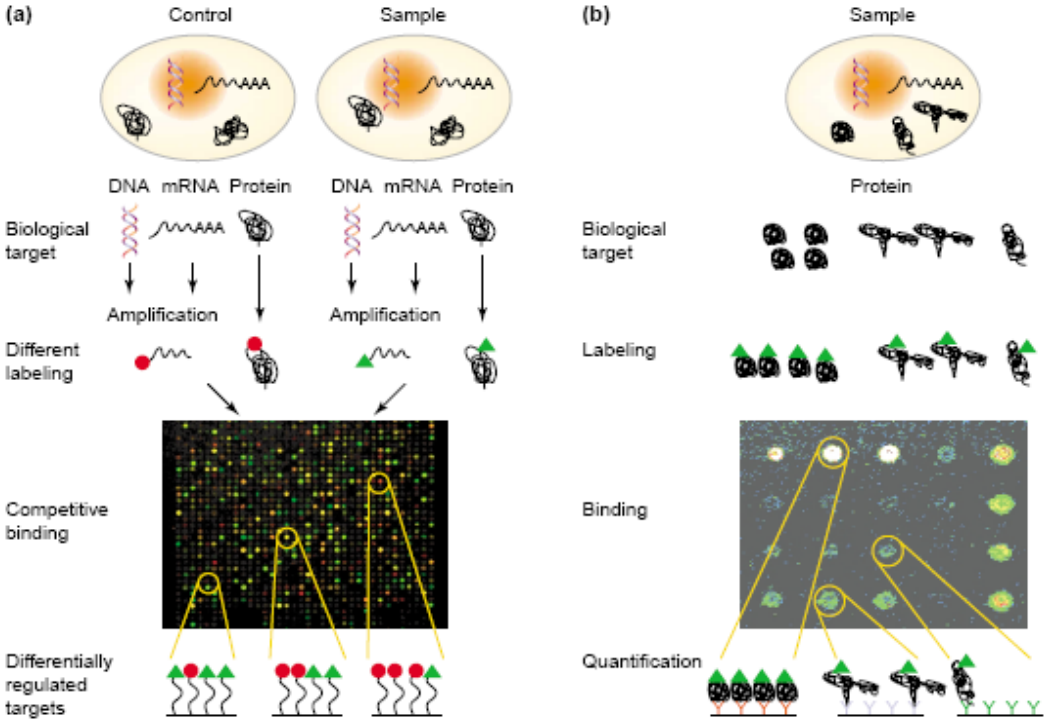

Figure **1-4**: Comparative and quantitative proteome analysis. (a) Comparative genome and proteome analysis, (b) parallel quantification of proteins [**13**].

Various biomolecular sensors based on this technology have been constructed [**9**][**10**][**11**] and have been claimed to be able to achieve detection limits of 10^7 molecules/cm^2 [**12**] thereby showing the extremely high sensitivity. In the case of the need for large amounts of detection such as in gene or protein recognition, chips based on

fluorescence probe have shown their utility by incorporating microarray technology (Figure **1-4**) [**13**][**14**][**15**][**16**]. However, the collected optical signal needs to be converted into an electrical format for easier processing, transmission, or digital storage afterwards. Therefore, these fluorescence based biomolecular sensors require highly accurate and expensive optical instruments to detect the extremely faint optical signal to realize the high sensitivity. Also sophisticated numerical algorithms are required to interpret the acquired data.

Furthermore, with these sensors based on fluorescence, light intensity-caused fluorescence changes termed photobleaching can be the factor limiting fluorescence detectability [**4**]. Photobleaching happens because the fluorophore molecules can be irreversibly modified or destroyed in the excited state and can therefore not be excited again resulting in loss of the emitted fluorescence light needed for detection. To overcome this problem, quantum dots based on quantum effects of semiconductor materials at the nano-scale, have been developed as substitutes for traditional organic fluorophores [**4**] (Figure **1-5**). An illustration of the photo-stability of quantum dots compared with traditional fluorescent dyes is shown in Figure **1-6**. As we can see, the fluorescence of traditional organic fluorophores decays with the time while quantum dots sustaining constant intensity. However, quantum dots are usually made of semiconductors with heavy metal components and the toxic nature of these quantum dots has been reported. In particular, they have been shown to cause cleavage effect in DNA or damage in biological tissues (Figure **1-7**) [**17**][**18**].

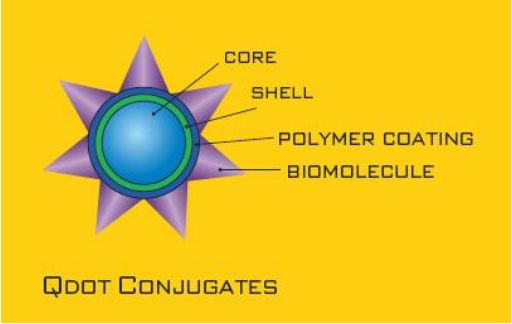

Figure **1-5**: The schematic of quantum dot structure [**4**].

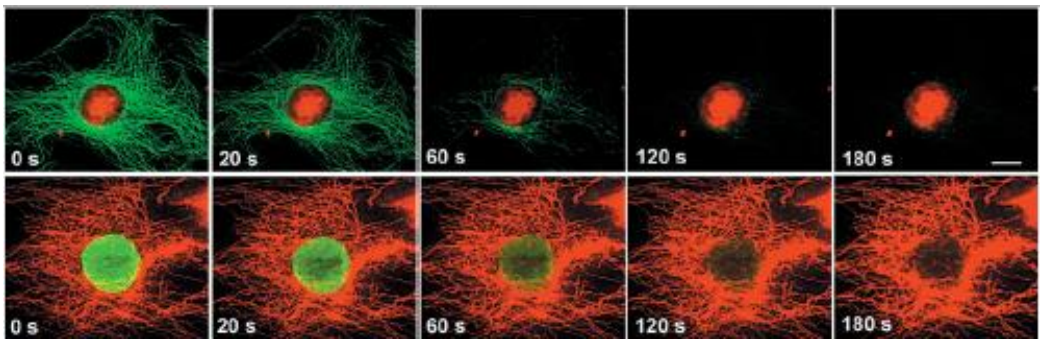

Figure **1-6**: Cell labeling with quantum dots and illustration of quantum dot photostability, compared with the fluorescence dye Alexa 488 [**4**].

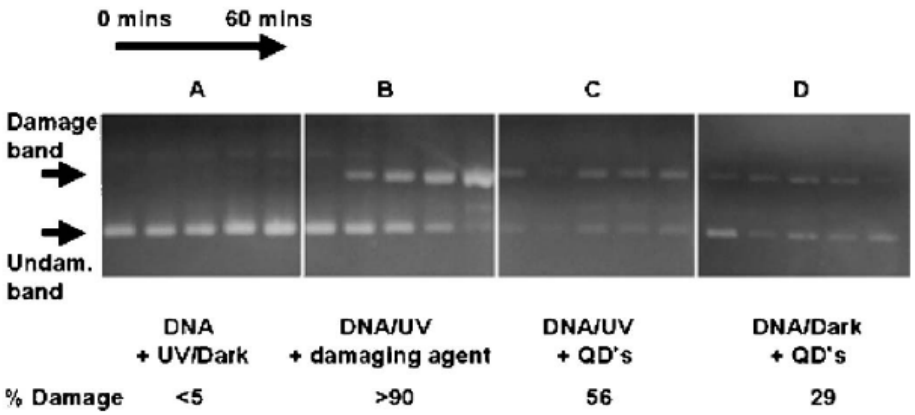

Figure **1-7**: Damage assays of DNA under different conditions. In each case, from left to right it shows result taken after every 15 min (0–60 min) [**17**].

1.1.2 Fluorescence-Label-Free Biomolecular Sensors

Recently, fluorescence-label-free biomolecular sensors, around as noted since the 1940s, have undergone rapid advances. These sensors directly utilize physical or chemical parameter changes induced by chemical reaction (e.g., between antigen and antibody). These technologies are usually relatively simple to implement and offer real-time/on-line detection. Optical, audio, electrical and thermal devices can all be used as the information transformation components.

Traditional fluorescence-label-free biomolecular sensors are based on easy physical parameter changes such as a mechanical signal (e.g., mass change), optical signal, and electrical signal, etc [**19**][**20**][**21**]. Novel fluorescence-label-free technologies such as surface plasmon resonance detection (SPR) [**22**][**23**], ion sensitive field effect transistor detection (ISFET) [**24**], light addressable potentiometric sensor detection (LAPS), surface acoustic wave detection (SAW), and quartz crystal microbalance detection (QCM) have been developed and utilized to build novel biomolecular sensors. Also, electrochemical based biomolecular sensors are well developed, under even further development, widely used, and function as one main category of biomolecular sensors.

1.1.2.1 Surface Plasmon Resonance Biomolecular Sensors

Surface plasmon resonance biomolecular sensors are highly sensitive, fast and stable sensors which are able to detect optical parameter changes. Detection relies on the affinity between the molecule to be detected and the metal substrate surface, which may be functionalized for specificity. The surface plasmon resonance phenomenon, also

known as surface plasmon polaritons, is based on the collective oscillation (plasmon) of the electrons in a metal. In thin films this can result in surface electromagnetic waves that propagate parallel along a metal/dielectric interface. In nano-particles [**22**], this collective oscillation sets up an intense near-field electromagnitic excitaion in a halo around the nano-particle. Usual metals that support surface and nano-particle plasmon are silver and gold.

In a typical SPR biomolecule sensing experiment, the probe molecule in the interactant molecular pairing is immobilized on a SPR-active gold coated glass slide, and the target molecule in an aqueous buffer solution is introduced to flow across this surface, by injecting it through the flow-cell (Figure **1**-**8**) [**23**]. When the light shines onto the gold surface at specific angles meeting the surface plasmon resonance condition, the light energy can be efficiently coupled into surface plasmon. And the optical reflectivity of gold changes extremely sensitively with the presence of biomolecules. This high sensitivity of the optical response is due to the fact that it is a very efficient, collective excitation of conduction electrons near the gold surface. The extent of binding between the solution-phase target molecule and the immobilized probe molecule is easily observed and quantified by monitoring this reflectivity changes.

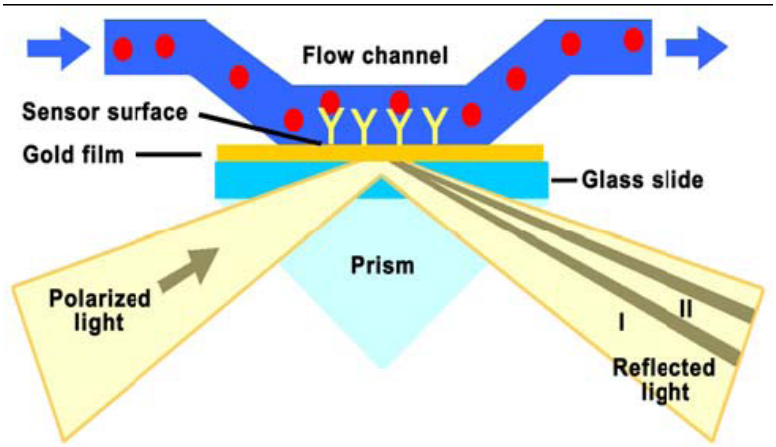

Figure **1-8**: The schematic of typical surface plasmon resonance sensor structure [**23**].

Also, the ability to monitor the forward and reverse reaction in real time offers this technology superior power for investigating the dynamical interaction between biomolecules. With the emergence of SPR technology, immunoassay process investigations have been significantly speeded-up [**25**]. With this technology, the dynamical interaction between DNA and protein was successfully investigated for the first time [**26**]. When used with Raman scattering and nano-particles, plasmons have proven to even be capable of single molecule detection [**22**].

The general SPR based analytical systems can only be realized with bulky external light generating and sensing instruments, until Texas Instruments developed the first low-cost and miniaturized biomolecule sensing platform SPREETA 2000 in 2003 (Figure **1-9**) [**27**]. However, the integration level is still low in view of the mm-scale size of the sensing area. And the surface spatial resolution for this category of analytical systems is yet to be improved.

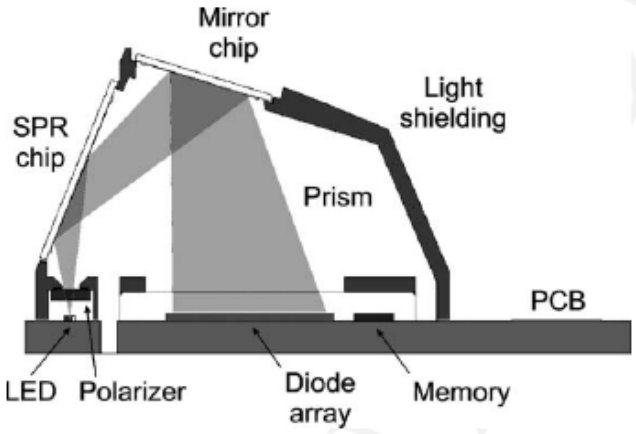

Figure **1-9**: Cross section of the SPREETA 2000 showing components of the sensor and the path followed by light inside the sensor [**27**].

1.1.2.2 Ion Sensitive Field Effect Transistor (ISFET) Biomolecular Sensors

A schematic of ion sensitive field effect transistor-based biomolecular sensor is shown in Figure **1-10** [**24**]. The basic structure is similar to the typical MOSFET except the gate connection is separated from the device and forms what is termed the reference electrode in electrochemistry. There is a gate dielectric present (silicon dioxide in Si-based ISFET) whose principal function is to passivate the Si surface and perform as the molecule binding/sensing surface. Other versions of this structure have been developed, but they are based on same principle. They either rely on current-voltage (I-V) curve shift in the case of the full ISFET or capacitance-voltage (C-V) curve shift in the case of a structure devoid of the source and drain. In either case, the shift is induced by the extra molecule charge attached on the dielectric surface during detection [**28**][**29**].

ISFET based biomolecular sensors are really stable, and they have fast response, high sensitivity, batch processing capability, micro-scale and the potential for on-chip circuit integration [**24**]. Through modifying the dielectric surface with diverse probe biomolecules, a variety of ISFET biosensors have been developed. Enzyme-linked FETs (ENFETs) have been developed by attaching the enzyme membrane on the gate dielectric layer [**30**][**31**]. Glucose concentration FET has been developed by attaching glucose oxidase on the gate dielectric layer [**32**]. A large number of affinitive biomolecular sensors have been developed which are based on immobilizing probe molecules on the gate dielectric layer [**33**][**34**][**35**].

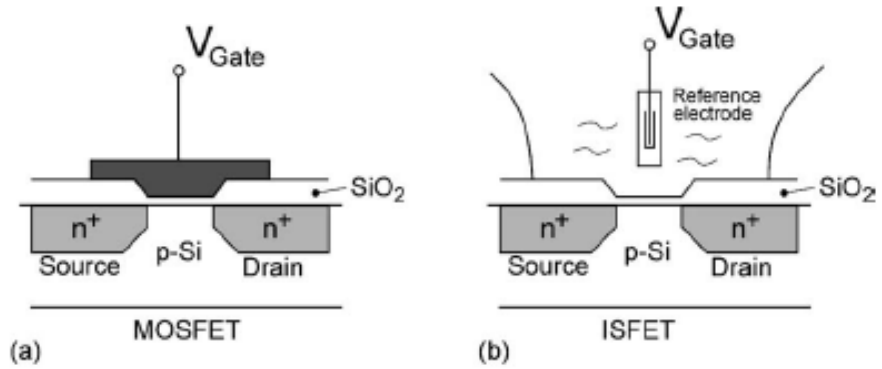

Figure **1-10**: The schematic of (a) MOSFET structure and (b) ISFET biomolecular sensor structure [**24**].

The main drawback of this category of biomolecular sensors is the corresponding large noise due to the electrical double layer in the electrolyte phase. Furthermore, these sensors are also quite responsive to background light noise which will reduce the device utility. Fabrication complexity including source and drain doping is another potential hindrance for further system application.

1.1.2.3 Light Addressable Potentiometric Biomolecular Sensors

Light addressable potentiometric (LAP) biomolecular sensors are also semiconductor-based (generally, silicon) sensors using light to activate excessive free carriers in semiconductor while selecting the activated spot where the measurement will be performed. Therefore, the surface potential distribution can be measured and spatially resolved by raster scanning a light-pointer along the surface. It is essentially the same as a charge couple device (CCD) array in functioning except the charge collecting wells are generated by the chemistry at the surface as opposed to being built-in as they are in a CCD. However it is much simpler in structure than a CCD. And it has been utilized to obtain gas reaction images for electro-olfactogram (EOG) and pH images [**36**][**37**].

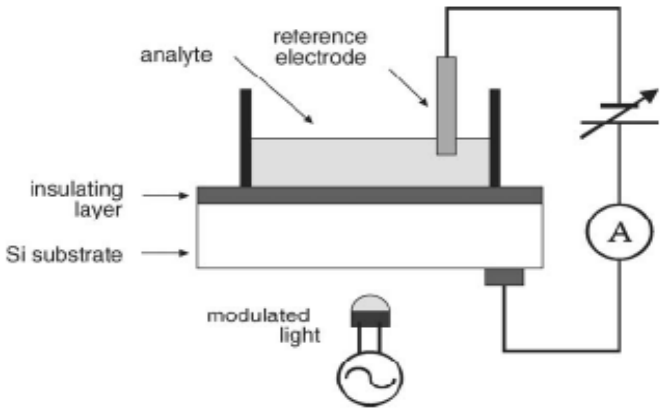

Figure **1-11**: The schematic of typical light addressable potentiometric sensor [**38**].

The typical schematic of LAPS is shown in Figure **1-11**. Its basic principle is based on the high sensitivity of semiconductor minority carrier populations to the potential change on the insulator and electrolyte interface, just as the case for CCD. The

modulated light emitted from the light source shines on the semiconductor and produces excessive free carriers (electrons and holes). These free carriers form the photoelectric current which causes carrier collection at the silicon/insulator interface. The carrier collection depends on the surface charge at the analyte/insulator interface. This surface charge change at the analyte/insulator interface can be detected by the reference electrode and amplified by a lock-in amplifier to realize high sensitivity. To fulfill the addressable ability, a scanning control system connected with light source is also required. This scanning control system is used to realize two dimensional movement of light source. To enable the detection of biomolecules, a molecule sensitive membrane is attached on the insulators. After target molecules attach onto the sensitive membrane and modify the surface potential at their positions, the membrane potential change due to the molecule attachment can be detected by measuring the photoelectric current.

Due to the extremely low photoelectric current to be detected and corresponding high background noise, special signal processing is required in LAPS. Generally a lock-in amplifier is utilized and an ac modulated frequency source is also required to realize the high sensitivity. Choosing an external light source is also a challenge when striving to develop a highly integrated analytical system.

1.1.2.4 Surface Acoustic Wave Based Biomolecular Sensors

A surface acoustic wave (SAW) is an acoustic wave traveling along the surface of a material having some elasticity, with an amplitude that typically decays exponentially with the depth of the substrate. This kind of wave is commonly used in piezoelectric

devices called SAW devices in electronic circuits. Surface acoustic wave biomolecular sensors use surface acoustic wave devices cotated with some molecule sensitive membranes for the detection of target molecules. Target molecule binding events are detected by the frequency shift caused by the mass change due to affinitive adsorption. These sensors can be used for detecting gases and liquids. A typical SAW device is shown in Figure **1-12**. Generally it consists of three parts on a piezoelectric substrate: transmitter (IDT1 in Figure **1-12**), medium, receiver (IDT2 in Figure **1-12**).

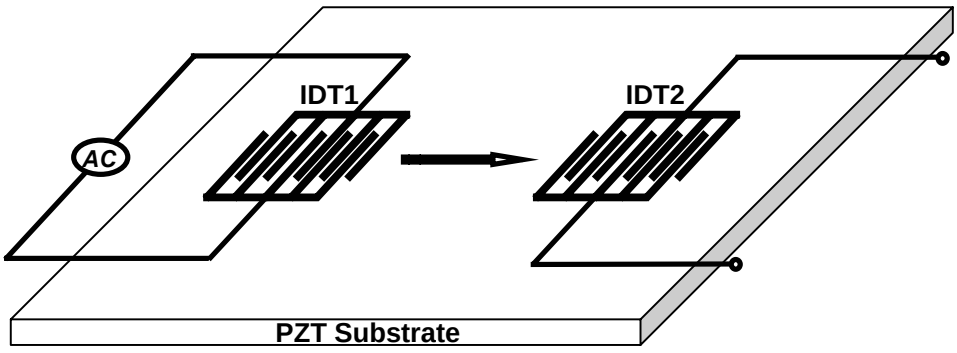

Figure **1-12**: The schematic of typical surface acoustic wave sensor.

In sensing, the acoustic wave is excited on the piezoelectric substrate by use of a metallic interdigital transducer (IDT1). The resulting wave is transmitted onto the substrate surface and received by the resonator of the other metallic interdigital transducer (IDT2). While the effect of any mass change due to attachment or adsorption on SAW propagation is the basis for detection, there are two different ways to essentially use SAW devices for sensing: the SAW resonator frequency changes or the SAW delay line time changes. Both of them are based on the influence of the surface mass on the

acoustic wave phase propagation speed. After probe molecules attach on the substrate sensing surface or the resonator part, the target molecules can be recognized by measuring the propagation resonance frequency or speed change [**39**][**40**].

However, multiple SAW sensors are not able to be simply integrated due to the coupling effect between two individual sensing devices. Further, the noise to signal ratio is high due to rapid wave signal decay and mechanical noise from the surrounding background.

1.1.2.5 Quartz Crystal Microbalance Biomolecular Sensors

Similar to surface acoustic wave biomolecular sensors, quartz crystal microbalance sensors are also piezoelectric devices. A typical sensor is made of quartz with electrodes evaporated on both sides of the crystal (Figure **1-13**). They are also extremely sensitive to mass change on the electrode surface due to the influence of mass on the mechanical vibration frequency.

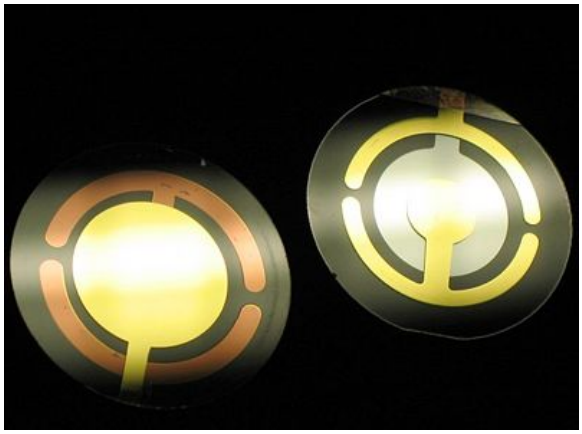

Figure **1-13**: Quartz crystal microbalance sensor [**41**].

The resonator frequency change (Δf) related with mass change (Δm) can be calculated with following equation [**42**]:

$$\Delta f = \frac{-2 f_0^2}{A\sqrt{\rho_q \mu_q}} \Delta m \qquad \textbf{1.1}$$

where f_0 is the intrinsic crystal frequency, A is the electrode area, ρ_q is the density of quartz, and μ_q is the shear modulus.

Based on this principle, clinical devices to detect viruses and proteins have been developed [**43**][**44**]. However, these quartz crystal microbalance sensors have their own disadvantages including the adverse influence of ambient temperature and humidity. And given the mm-scale size, the integration level will not be adequately high.

1.1.2.6 Electrochemical Biomolecular Sensors

Since the world's first biomolecular sensor based on an electrochemical reaction - the enzyme electrode - to detect glucose concentration was reported in 1960s, significant technology advances have been applied in this field including electrode optimization and minimization, etc. Traditional electrochemical biomolecular sensors are either amperometric or potentiometric sensors which require accurate current or voltage measurement cross the electrode-electrolyte interface. However, the electrical double layer existing on the electrode surface interferes with the accuracy of these measurements. Generally, to achieve best signal to noise ratio or maximize the performance of the system, a typical three electrode setup is utilized (Figure **1-14**) [**45**]. The reference

electrode is required to be a quasi-non-polarizable electrode without charge accumulation, therefore, is able to work as a potential reference point in the electrolyte. This strict requirement of reference electrode makes this setup not suitable for further higher integration due to fabrication complexity. The working electrode provides the surface where the chemical reaction between probe and target molecules happens and, in the amperometric version, it conducts the electrical current which is the indicator of the reaction and, hence, the concentration of the target molecules.

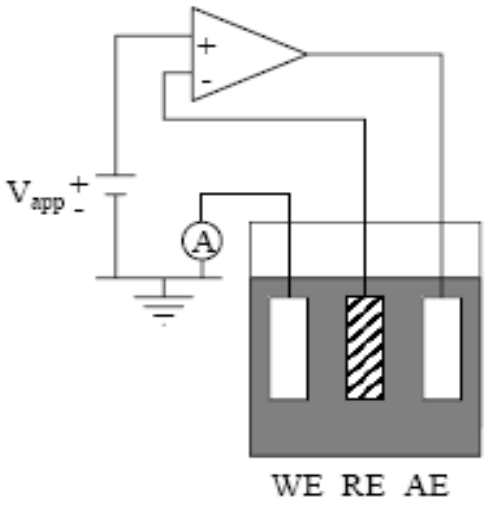

Figure **1-14**: The schematic of typical three electrode setup [**45**].

Among all different kinds of electrochemical biomolecular sensors, DNA sensors are one of the most representative categories. There are several versions: direct electrochemical sensor [**46**][**47**], indirect electrochemical sensor [**48**], DNA-specific redox indicator sensor [**49**][**50**], nano-particle based sensor [**51**][**52**], and DNA-mediated

charge sensor [**53**][**54**]. A comprehensive review and comparison of current electrochemical DNA sensors is presented in Table **1-1** [**55**].

Table **1-1**: Comparison of platforms for DNA electrochemical sensing [**55**].

Type of Sensor	Advantages	Disadvantages
Direct DNA electrochemistry	Highly sensitive; requires no labeling step; amenable to a range of electrodes	High background signals; cannot be multiplexed; destroys the sample
Indirect DNA electrochemistry	Highly sensitive; usually requires no labeling step; multiple-target detection at same electrode	Probe substrate can be difficult to prepare; destroys the sample
DNA-specific redox indicator detection	Moderate to high sensitivity; well suited to multiple-target detection; samples remain unaltered	Chemical labeling step required unless sandwich method used; sequence variations can be problematic
Nano-particle-based electrochemistry amplification	Extremely sensitive; well suited to multiple-target detection with different nanoparticles	Many development steps in assay; reliability and robustness of surface structures problematic; sample usually destroyed
DNA-mediated charge transport	Highly sensitive and simple assay; requires no labeling; uniquely well suited for mismatch detection; sequence independent; amenable to multiplexing	Biochemical preparation of target sample require

Electrochemical biomolecular sensors are advantageous in that no signal conversion is required since the signal is acquired directly as electrical excitation resulting from the chemical reaction of interest. This can be applied to achieve extremely high integration level, especially as microarray sensor design becomes more sophisticated. On the other hand, electrochemical interactions between solid surfaces and an electrolyte phase are not completely understood. Furthermore, the noise due to the presence of an

electrical double layer in the electrolyte can be a problem for most of electrochemical analytical systems.

1.2 Nano-Gap Electrical Biomolecular Sensors

Nano-gap biomolecular sensors are a new type of sensor approach that has just come forth in the past decade [**56**][**57**]. They are of interest because they offer the possibility of circumventing the current biomolecular sensor limitations outlined above. Most of the current commercialized systems use an optical method as the main detection principle and thereby necessitate the assistance of highly sophisticated optical instruments and optical-to-electrical signal conversion. This is a technical bottleneck impeding future highly integrated analytical systems. To circumvent this problem, considerable research has been focused on electrochemical approaches.

Nano-gap sensing structures using electrical impedance or DC current sensing have recently been reported. Several different systems and their application to biomolecule detection have been disclosed with either a semiconductor or metal as the electrode [**58**][**59**][**60**]. In the case of the ac impedance version, there is an advantage of noise minimization due to the unique nano-gap structure which causes the two opposite electrical diffuse layers to overlap. Theoretical modeling has been presented to explain this advantage [**61**]. However, these analyses are yet not comprehensive and precise enough and not especially beneficial in device design. Therefore, to take full advantages of this novel nano-gap sensing structure, a thorough understanding of the theoretical principle behind it is required.

Another challenge in current nano-gap biomolecular sensor development is that these sensors still lack an integrated nanofluidic flow control component for active flow control which is absolutely necessary to fulfill requirements of future analytical systems. Most of the approaches tried to-date are based on a passive diffusion mode [**62**], and some of them even work under dry conditions [**63**] which is extremely impractical.

1.3 Dissertation Organization and Contributions

In this dissertation, a sub-50 nm direct electrical capacitor sensing structure integrated with micro- and nano-fluidic flow control components is presented (Figure **1-15**). The device is based on a full analysis, design and fabrication approach, which addresses noise, sensitivity, and integration issues.

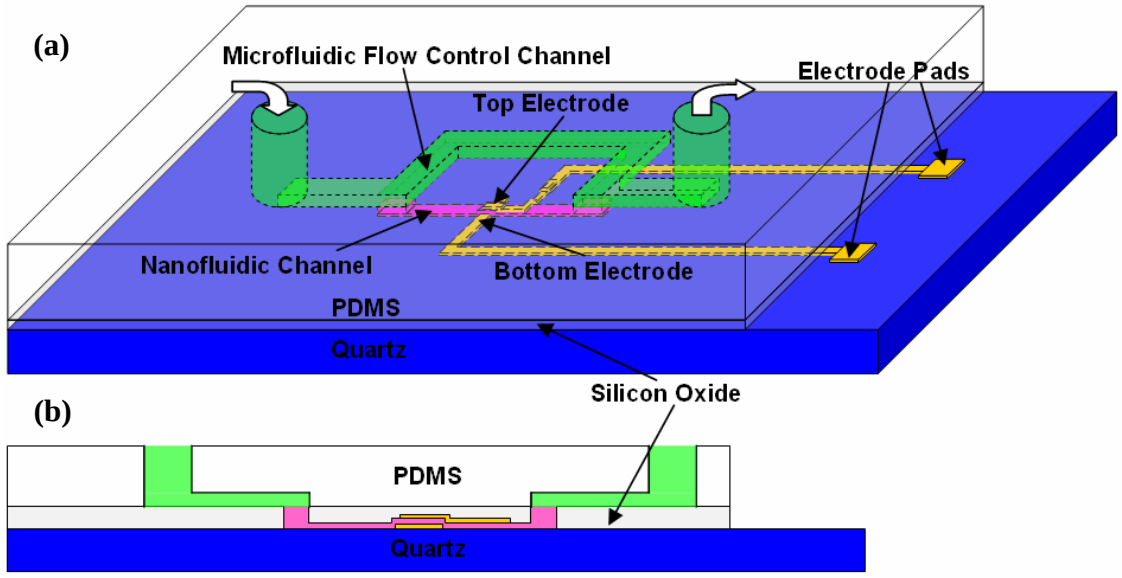

Figure **1-15**: The schematic of the nano-gap biomolecular sensor: (a) top view and (b) cross-sectional view. Green path represents microfluidic flow in PDMS, and purple represents nanofluidic flow through the nano-gap sensing structure.

The device is composed of a microfluidic flow control channel in PDMS and a nanofluidic channel in silicon oxide which are all integrated with a nano-gap sensing structure. This is the first time it has been accomplished, to our knowledge. The microfluidic flow control channel in PDMS provides access to the nanofluidic channel feeding the nano-gap sensing structure by connecting with nanofluidic channel in parallel. By using the parallel flow control configuration for interfacing with the outside world, active fluidic flow and exchange through the nanofluidic channel is able to be achieved. This parallel flow control configuration also provides accurate flow rate control through the nanofluidic channel. The nano-gap sensing region itself in our device has been designed and optimized based on a detailed theoretical analysis. A result of this analysis is our being able to reduce electrochemical background noise.

To demonstrate the feasibility of parallel flow control approach utilized in our biomolecule detection system, individual nanofluidic flow control devices based on glass etching and bonding are also demonstrated in this dissertation. The parallel flow control approach has proven to be able to accomplish very fine nanofluidic flow control and be able to measure the nanofluidic flow rate exceeding the current lowest limit reported in literature.

This dissertation consists of 6 chapters. The first chapter is the just-completed brief review of biomolecular sensors and the future development trend. The second chapter is the experiment design chapter which includes the fundamental theoretical analysis of electrochemical interaction in the nano-gap sensing structure and parallel flow control approach. The third chapter gives the system fabrication, consisting of parallel

flow control demonstration devices and a complete biomolecular sensor composed of nano-gap sensing structure integrated with nanofluidic flow control components. The forth chapter presents the experiment results of the novel parallel flow control approach for nanofluidics. In chapter 5, an application demonstration of the integrated analytical system to biomolecule detection is presented. The future direction of the work is discussed in chapter 6.

The contribution of this research includes:

1. Theoretical investigation of the novel parallel flow control approach for nanofluidic control.
2. Design and fabrication of novel parallel flow control devices for nanofluidic control.
3. Theoretical investigation of the electrochemical interaction in a nano-gap sensing structure.
4. Design and fabrication of a novel nano-gap electrical capacitance biomolecular sensor with integrated nanofluidics.
5. Demonstration of this integrated analytical system in biomolecule detection.

References

1. J.W. Severinghaus, and P.B. Astrup, "History of Blood Gas Analysis. IV. Leland Clark's Oxygen Electrode," *Journal of Clinical Monitoring and Computing* **2:** 125-139, (1986)

2. J.R. Lakowicz, *Topics in Fluorescence Spectroscopy: Biochemical Applications.* Plenum Publishing, New York, NY (1992)

3. W.T. Mason, *Fluorescent and Luminescent Probes for Biological Activity. 2nd ed.* Academic Press, San Diego, CA (1999)

5. S. Weiss, "Fluorescence Spectroscopy of Single Biomolecules," *Science* **283:** 1676-1683, (1999)

6. B. Herman, X.F. Wang, A. Periasamy, S. Kwon, G.W. Gordon, and P. Wodnicki, "Fluorescence Lifetime Imaging in Cell Biology," *Proceedings of SPIE* **2678:** 88-97, (1996)

7. R.M. Hoffman, "*In Vivo* Imaging with Fluorescent Proteins: the New Cell Biology," *Acta Histochemica* **106:** 77-87, (2004)

8. R.M. Hoffman, "Imaging Cellular Dynamics *In Vivo* with Multi-color Fluorescent Proteins," *Proceedings of SPIE* **5704:** 146-157, (2005)

4. R.P. Haugland, *Handbook of Fluorescent Probes and Research Products.* Molecular Probes, Inc., Eugene, OR (2002)

9. Y.K. Yen, J.Y. Lee, M.C. Kuo, and L.S. Huang, "The Application of an Innovative MEMS Protein Chip in Real-time Total Internal Reflection Fluorescence Microscopy," *Proceedings of the 2005 IEEE International Conference on Mechatronics* pp: 280-283, (2005)

10. J.R. Webster, M.A. Burns, D.T. Burke, and C.H. Mastrangelo, "Electrophoresis System with Integrated On-chip Fluorescence Detection," *Proceedings of the 13th Annula IEEE International MEMS Conference* pp: 306-310, (2000)

11. X. Wang, and J.K. Ulrich, "A Self-contained Fluorescent Fiber Optic DNA Biosnsor," *Journal of Materials Chemistry* **15:** 2801-2809, (2005)

12. J.R. Epstein, I. Biran, and D.R. Walt, "Fluorescence-based Nucleic Acid Detection and Microarrays," *Analytica Chimica Acta* **469:** 3-36, (2002)

13. M.F. Templin, D. Stoll, M. Schrenk, P.C. Traub, C.F. Vohringer, and T.O. Joos, "Protein Microarray Technology," *TRENDS in Biotechnology* **20:** 160-166**,** (2002)

14. J. Jacak, J. Hesse, C. Hesch, M. Kasper, F. Aberger, A. Frischauf, M. Sonnleitner, G. Freudenthaler, S. Howorka, and G.J. Schutz, "Ultra-sensitive DNA Detection on Microarrays," *Proceedings of SPIE* **5699:** 442-449, (2005)

15. H.G. Park, J.Y. Song, K.H. Park, and M.H. Kim, "Fluorescence-based Assay Formats and Signal Amplification Strategies for DNA Microarray Analysis," *Chemical Engineering Science* **61:** 954-965, (2006)

16. A. Jung, "DNA Chip Technology," *Analytical and Bioanalytical Chemistry* **372:** 41-42, (2002)

17. M. Green, and E. Howman, "Semiconductor Quantum Dots and Free Radical Induced DNA Nicking," *Chemical Communications* pp: 121-123, (2005)

18. R. Hardman, "A Toxicologic Review of Quantum Dots: Toxicity Depends on Physicochemical and Environmental Factors," *Environmental Health Perspectives* **114:** 165-172, (2006)

19. F.W. Scheller, F. Schubert, R. Renneberg, and H.G. Muller, "Biosensors: Trends and Commercialization," *Biosensors* **1:** 135-160, (1985)

20. P. Poscio, C. Depeursinge, "Realization of a Miniaturized Optical Sensor for Biomedical Applications," *Sensors and Actuators A* **23:** 1092-1096, (1990)

21. P. Bergveld, "A Critical Evaluation of Direct Electrical Protein Detection Methods," *Biosensors & Bioelectronics* **6:** 55-72, (1991)

22. A.K. Kalkan, and S.J. Fonash, "Laser-activated Surface-enhanced Raman Scattering Substrates Capable of Single Molecule Detection," *Applied Physics Letter* **89:** 233103, (2006)

23. M.A. Cooper, "Label-free Screening of Bio-molecular Interactions," *Analytical and Bioanalytical Chemistry* **377:** 834-842, (2003)

24. P. Bergveld, "Thirty Years of ISFETOLOGY What Happened in the Past 30 Years and What May Happen in the Next 30 Years," *Sensors and Actuators B* **88:** 1-20, (2003)

25. W.M. Mullett, E.P. Lai, and J.M. Yeung, "Surface Plasmon Resonance-based Immunoassays," *Methods* **22:** 77-91, (2000)

26. V. Silin, and A. Plant, "Biotechnological Applications of Surface Plasmon Resonance," *Trends in Biotechnology* **15:** 353-359, (1997)

27. T.M. Chinowsky, J.G. Quinn, D.U. Bartholomew, R. Kaiser, and J.L. Elkind, "Performance of the Spreeta 2000 Integrated Surface Plasmon Resonance Affinity Sensor," *Sensors and Actuators B* **6954:** 1-9, (2003)

28. W. Yang, and R.J. Hamers, "Fabrication and Characterization of a Biologically Sensitive Field-Effect Transistor Using A Nanocrystalline Diamond Thin Film," *Applied Physics Letters* **85:** 3626-3628, (2004)

29. P. Estrela, P. Migliorato, H. Takiguchi, H. Fukushima, and S. Nebashi, "Electrical Detection of Biomolecular Interactions with Metal-insulator-semiconductor Diodes," *Biosensors and Biolelectronics* **20:** 1580-1586, (2005)

30. C. Colapicchioni, A. Barbaro, and F. Porcelli, "Fabrication and Characterization of ENFET Devices for Biomedical Applications and Environmental Monitoring," *Sensors and Actuators B* **6:** 202-207, (1992)

31. K. Wan, J.M. Chovelon, N. J. Renault, and A.P. Soldatkin, "Sensitive Detection of Pesticide Using ENFET with Enzymes Immobilized by Cross-linking and Entrapment Method," *Sensors and Actuators B* **58:** 399-408, (1999)

32. V.K. Khanna, A. Kumar, Y.K. Jain, and S. Ahmad, "Design and Development of a Novel high-transconductance pH-ISFET (Ion-sensitive Field-effect Transistor)-based Glucose Biosensor," *International Journal of Electronics* **93:** 81-96, (2006)

33. S. Alegret, J. Bartroli, C. Jimenez, E. Martinez-Fabregas, D. Martorell, and F. Valdes-Perezqasqa, "ISFET-based Urea Biosensor," *Sensors and Actuators B* **16:** 453-457, (1993)

34. M.L. Pourciel-Gouzy, W. Sant, I. Humenyuk, L. Malaquin, X. Dollat, and P. Temple-Boyer, "Development of pH-ISFET Sensors for the Detection of Bacterial Activity," *Sensors and Actuators B* **103:** 247-251, (2003)

35. L. Campanella, C. Colapicchioni, M. Tomasetti, A. Bianco, and S. Dezzi, "A New ISFET Device for Cocaine Analysis," *Sensors and Actuators B* **24:** 188-193, (1995)

36. F. Winquist, H. Sundgren, E. Hedborg, and I. Lundstrom, "Evaluation of Gas Sensing Surfaces with a Scanned Light Pulse Technique," *Sensors and Actuators B: Chemical* **16:** 270-274, (1993)

37. S.R. Manalis, and E.B. Cooper, "Microvolume Field-effect pH Sensor for the Scanning Probe Microscope," *Applied Physics Letters* **76:** 1072-1074, (2000)

38. T. Wagner, T. Yoshinobu, C. Rao, R. Otto, and M.J. Schoning, "All-in-one Solid-state Device Based on a Light-addressable Potentiometric Sensor Platform," *Sensors and Actuators B* **117:** 472-479, (2006)

39. K. Lange, A. Voigt, and M. Rapp, "Surface Acoustic Wave Biosensors for Biomolecular Interaction Analysis," *Proceedings of IEEE* **2:**1174-1178, (2003)

40. E. Benes, M. Groschl, F. Seifert, and A. Pohl, "Comparison between BAW and SAW Sensor Principles," *IEEE Transactions on Ultrasonics, Ferroelectrics, and Frequency Control* **45:** 1314-1329, (1998)

41. Brims Ness Corporation. www.brimsness.com

42. K.A. Marx, "Quartz Crystal Microbalance: A Useful Tool for Studying Thin Polymer Films and Complex Biomolecular Systems at the Solution-Surface Interface," *Bioacromolecules* **4:** 1099-1120 (2002)

43. J. Rickert, T. Weiss, W. Kraas, G. Jung, and W. Goepel, "A New Affinity Biosensor: Self-assembled Thiols as Selective Monolayer Coatings of Quartz Crystal Microbalances," *Biosensors and Bioelectronics* **11:** 591-598, (1996)

44. J. Wang, M. Jiang, and E. Palecek, "Real-time Monitoring of Enzymatic Cleavage of Nucleic Acids Using a Quartz Crystal Microbalance," *Bioelectrochemistry and Bioengergetics* **48:** 477-480, (1999)

45. J.D. Zahn, A.A. Deshmukh, A.P. Papavasiliou, A.P. Pisano, and D. Liepmann, "An Integrated Microfluidic Device for the Continuous Sampling and Analysis of Biological Fluids," *Proceedings of 2001 ASME International Mechanical Engineering Congress and Exposition* pp: 1-6, (2001)

46. E. Komarova, M. Aldiss, and A. Bogomolova, "Direct Electrochemical Sensor for Fast Reagent-free DNA Detection," *Biosensors and Bioelectronics* **21:** 182-189, (2005)

47. N. Lassalle, P. Mailley, E. Vieil, T. Livache, A. Roget, J.P. Correia, and L.M. Abrantes, "Electronically Conductive Polymer Grafted with Oligonucleotides as Electrosensors of DNA," *Journal of Electroanalytical Chemistry* **509:** 48-57, (2001)

48. I.V. Yang, and H.H. Thorp, "Modification of Indium Tin Oxide Electrodes with Repeat Polynucleotides: Electrochemical Detection of Trinucleotide Repeat Expansion," *Analytical Chemistry* **73:** 5316-5322, (2001)

49. J.J. Summer, K.W. Plaxco, C.D. Meinhart, and H. Soh, "Development of an Electrochemical Biosensor without a Sandwich Assay," *Proceedings of SPIE* **6007:** 61-66, (2005)

50. C.J. Yu, Y. Wan, H. Yowanto, J. Li, C. Tao, M.D. James, C.L. Tan, G.F. Blackburn, and T.J. Meade, "Electronic Detection of Single-base Mismatches in DNA with Ferrocene-modified Probes," *Journal of American Chemistry Society* **123:** 11155-11161, (2001)

51. C.Y. Tsai, T.L. Chang, C.C. Chen, F.H. Ko, and P.H. Chen, "An Ultra Sensitive DNA Detection by Using Gold Nanoparticle Multilayer in Nano-gap Electrodes," *Microelectronic Engineering* **78:** 546-555, (2005)

52. J. Wang, R. Polsky, A. Merkoci, and K.L. Turner, "Electroactive Beads for Ultrasensitive DNA Detection," *Langmuir* **19:** 989-991, (2003)

53. X. Li, J.S. Lee, and H.B. Kraatz, "Electrochemical Detection of Single-Nucleotide Mismatches Using and Electrode Microarray," *Analytical Chemistry* **78:** 6096-6101, (2006)

54. J.G. Kushmerick, D.B. Holt, J.C. Yang, J. Naciri, M.H. Moore, and R. Shashidhar, "Metal-molecule Contacts and Charge Transport across Monomolecular Layers: Measurement and Theory," *Physical Review Letters* **89:** 0868021-0868024, (2002)

55. T.G. Drummond, M.G. Hill, and J.K. Barton, "Electrochemical DNA Sensors," *Nature Biotechnology* **21:** 1192-1199, (2003)

56. T.L. Chang, C.Y. Tsai, C.C. Sun, R. Uppala, C.C. Chen, C.H. Lin, and P.H. Cheng, "Electrical Detection of DNA using Gold and Magnetic Nanoparticles and Bio Bar-code DNA between Nanogap Electrodes," *Microelectronic Engineering* **84:** 1630-1633, (2006)

57. C. Zanetti, J.T. Nevill, D.D. Carlo, K.H. Jeong, and L.P. Lee, "Nanogap Capacitors: Sensitivity to Sample Permittivity Changes," *Journal of Applied Physics* **99:** 0243051-0243055, (2006)

58. A. Malave, M. Tewes, T. Gronewold, and M. Lohndorf, "Development of Impedance Biosensors with Nanometer Gaps for Marker-free Analytical Measurements," *Microelectronic Engineering* **78:** 587-592, (2005)

59. D.D. Carlo, H. Kang, X. Zeng, K.H. Jeong, and L.P. Lee, "Nanogap-based Dielectric Immunosensing," *The 12th International Conference on Solid State Sensors, Actuators and Microsystems* pp: 1180-1183, (2003)

60. H.K. Kang, J. Seo, D.D. Carlo, Y.K. Choi, and L.P. Lee, "Planar Nanogap Capacitor Arrays on Quartz for Optical and Dielectric Bioassays," *7th International Conference on Miniaturized Chemical and Biochemical Analysis Systems* pp: 697-700, (2003)

61. M. Yi, K.H. Jeong, and L.P. Lee, "Theoretical and Experimental Study towards a Nanogap Dielectric Biosensor," *Biosensors and Bioelectronics* **20:** 1320-1326, (2005)

62. W.J. Nam, J.D. Cuiffi, and S.J. Fonash, "Fabrication of Evaluation of Highly Manufacturable Nanoscale Flow-through Parallel Electrode Structures," *Journal of Vacuum Science and Technology B: Microelectronics and Nanometer Structures* **22:** 35-37, (2004)

63. J.S. Lee, Y.K. Choi, M. Pio, J. Seo, and L.P. Lee, "Nanogap Capacitors for Label Free DNA Analysis," *Proceedings of Material Research Society Symposium* **729:** 185-190, (2002)

Chapter 2

Experiment Design

The goal of this work is to implement a nano-gap biomolecule capacitance sensor system with nanofluidic control. This implementation necessitates understanding of the electrochemical dynamics of the electrical double layer in such a nano-gap sensing device which forms upon exposure to the electrolyte, and the impact of changes in this double layer on device electrical properties; i.e., DC current and AC capacitance. Implementation also requires the full understanding of how to actively control the fluid flow through the nano-gap sensing structure.

A theoretical analysis of the electrical double layer configuration between nano-gap electrodes is presented based on conventional electrostatics and thermodynamics. The new fact explored here is what happens when the electrical double layer thickness predicted on the basis of electrolyte concentrations and metal electrode work functions is of the order of, or larger than, the nano-scale gap spacing. The resulting diffuse layer overlapping due to the nano-scale of the physical shielding length is studied to show how our nano-gap sensing device can achieve enhanced capacitance sensitivity by shielding unwanted electrochemical noise. A schematic model and corresponding theoretical analysis are performed to show the noise shielding advantages in nano-gap sensing structures. This analysis is then used as a guide for our device design.

In addition, the issues of flow and pressure gradients through the nano-gap sensing structure are also a focus of this work. The active molecule flow and exchange

through the nano-gap sensing structure is fundamentally required for implementing a rapidly responsive biomolecular sensor. These issues are solved using a novel nanofluidic parallel flow control component initially developed using a theoretical analysis to support its feasibility. With the approach developed in this dissertation, an active nanofluidic flow control is achieved using a microfluidic flow control channel connected with the nanofluidic channel in parallel. By using this unique parallel connection configuration, an extremely finely controlled flow rate through the nanofluidic channel leading to and from the nano-gap sensing structure is realized and the interfacing problems with the external macro-fluidic world are solved successfully.

2.1 Fundamentals of Nano-Gap Electrochemical Interaction

Electrochemical double layer formation between an ionic solution and a solid conductor (e.g., metal) electrode has been studied for longer than a century. The resulting interface produces what is termed an electrical double layer. This double layer is basically due to the electrochemical potential difference between the solid surface and the electrolyte. This potential difference induces electrons, holes, or both to redistribute in the solid electrode and ions to redistribute in the electrolyte. Typically, the ion rearrangement region in the electrolyte phase may be thought of as consisting of two layers - an inner layer and an outer layer (Figure **2-1**) which gives rise to the term of electrical double layer. The inner layer is called as the compact, Helmholtz, or Stern layer. It is ascribed to a thin monolayer of ions absorbed on the electrode surface. The outer

layer is called the diffuse layer. It extends from the inner layer into the bulk solution region defined as where full electrostatic shielding is accomplished.

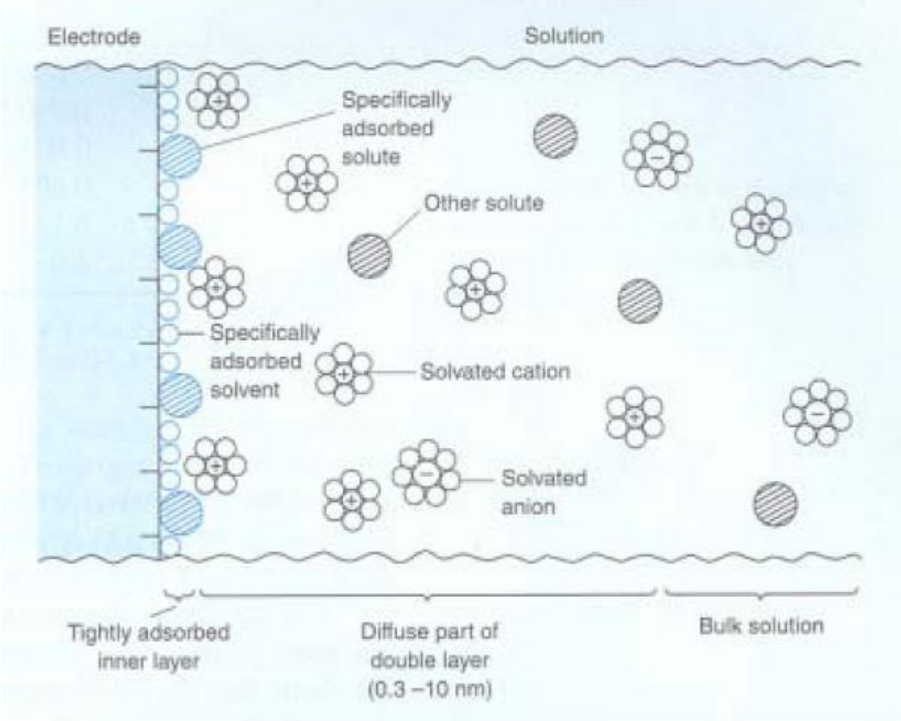

Figure **2-1**: The schematic of electrical double layer [**1**].

After formation, this electrical double layer can be modified with the application of an AC, DC, or both perturbing biasing condition. Such a perturbation drives the electrode/electrolyte system out of originally thermodynamic equilibrium. Many models have been put forward to explain the behavior observed when electrochemical measurements are performed on such perturbed electrode/electrolyte systems. The earliest model of the thermodynamic equilibrium electrical double layer is usually attributed to Helmholtz (1879) [**2**][**3**]. Helmholtz treated the double layer mathematically as a simple capacitor, based on a physical model in which a single layer of ions is

adsorbed at the surface. Later Gouy and Chapman (1910-1913) made significant improvements by introducing a diffuse model of the electrical double layer, in which the potential at a surface decreases exponentially due to a shielding region of counter-ions from the solution [**4**][**5**]. The current classical electrical double layer model is termed the Gouy-Chapman-Stern model, which combines the Helmholtz single adsorbed layer with the Gouy-Chapman diffuse layer [**6**].

These models are traditionally applied to a single electrode/electrolyte pairing; i.e., it is assumed that the electrical double layer thickness is small compared to the inter-electrode spacing. Up to now, there is a dearth of analysis examining electrical double layer formation in nano-gap capacitor structures. In nano-scale domain, the diffuse layers from the two opposite electrodes begin to overlap each other. If both electrodes are made of same material, these electrical double layers will be dimensionally symmetrical. The overlapping of such symmetrical diffuse layers will cause ion rearrangement and can generate modifications in behavior of the perturbed state. In the following section we will present a theoretical analysis of electrochemical interaction in a nano-gap capacitor structure at thermodynamic equilibrium to assess the impact of electrical double layer overlapping.

In this research effort, molecule detection capability is based on taking control of the components of Helmholtz layer to induce the electrical capacitance change upon probe and target molecule binding on the gold electrode surfaces (spaced 50 nm) in the nano-gap sensing structure. A simple theoretical analysis model and corresponding electric circuit model are given in Figure **2-2**. Figure **2-2.a** shows the ionic distribution between two nano-gap gold electrode surfaces each with a self-assembled monolayer

(SAM) of probe and target molecules present. Corresponding capacitance circuit model with relevant capacitor components due to the SAM (C_{SAM}) and electrical diffuse layer (C_D) are shown in Figure **2-2.b**. From the electric circuit model, we have

$$C_{Total} = C_{SAM} C_D / 2\left(C_{SAM} + C_D\right) \qquad \textbf{2.1}$$

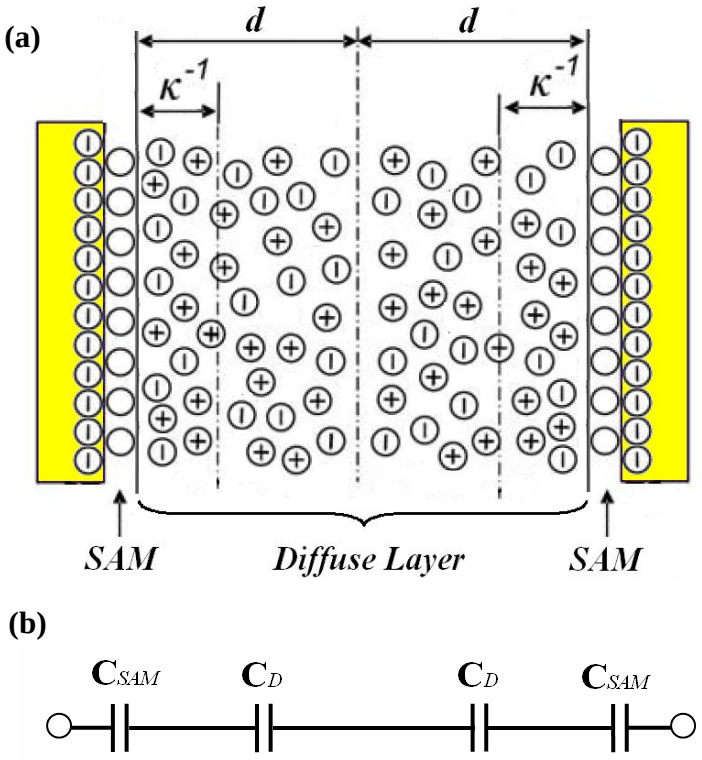

Figure **2-2**: (a) Schematic diagram of the ion distribution between two nano-gap gold electrodes without external voltage, and (b) corresponding electric circuit model.

Our detection scheme is set up such that any attached biomolecule would change the C_{SAM} value, and, therefore, change the measured capacitance value C_{Total}. From Eq. **2.1**, it is clear that system sensitivity to any biomolecule attachment can be

optimized by maximizing diffuse layer capacitance C_D. Figure **2-3**, which shows the total measured capacitance C_{Total} with different values of the capacitance ratio C_{SAM}/C_D, makes this point. As we can see, this simple analysis indicates the system will perform best when C_{SAM}/C_D goes to zero (blue line); in other words, we need to maximize C_D. This can be realized by using high concentration ionic solutions; however, it is incompatible with the biomolecules being sensed given the chemical damage it may cause.

The alternative approach used here is to overlap the electrical double layers extended from the two opposite gold electrode surfaces by shrinking the electrode distance (~2d) down to the characteristic thickness of the diffuse layer ($\kappa^{-1} = \left(2n^0 z^2 e^2 / \varepsilon\varepsilon_0 kT\right)^{-1/2}$). This overlapping will cause C_D increase dramatically and reduce the unwanted capacitance noise. To demonstrate the biomolecule sensing capabilities of nano-gap sensing devices, probe and target molecules (cysteamine and quantum dots) in electrolyte solution will be infused through the system to be assembled and bonded on the gold electrode surfaces consecutively. Following each binding step, DI water with a characteristic thickness of diffuse layer (κ^{-1}) around 1 μm is specifically selected and infused to flush away the unspecifically attached molecules and unwanted ionic components from the previous infusion. Subsequently, electrical measurement can be done with DI water as the electrical measurement medium to fulfill the diffuse layer overlapping condition, and take advantages of noise shielding.

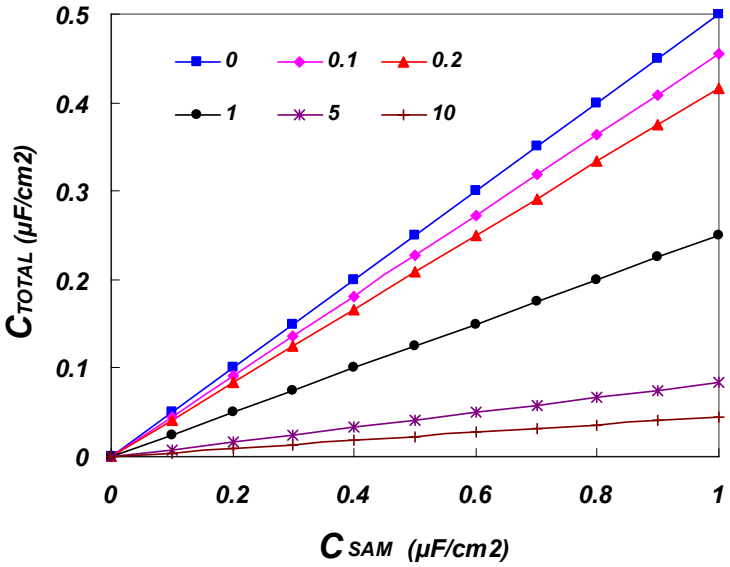

Figure **2-3**: The theoretical analysis results of C_{Total} against C_{SAM} with different capacitance ratio values of C_{SAM}/C_D. As we can see, the system performs best when C_{SAM}/C_D goes to zero; i.e., it performs best by maximizing C_D. Here C_{SAM} is the capacitance of self-assembled monolayer and C_D is the capacitance of electrical double layer.

2.2 Fundamentals of Active Nanofluidic Flow Control

In the past two decades, there has been a major research effort directed toward the development of Micro-Total Analysis Systems (μTAS) [**7**][**8**] and, more recently, also toward the development of miniaturized chemical processing systems [**9**][**10**][**11**]. Among these, microfluidic systems have been fully studied and to-day function as an absolutely necessary component in various kinds of analytical systems. The analytical systems are now rapidly moving toward the use of nanofluidics to exploit smaller sample size, potentially precise flow control, and new sensing approaches [**12**][**13**][**14**]. The

chemical processing work is also rapidly moving toward the use of nanofluidics to exploit mixing and reaction effects at the nano-scale [**15**][**16**]. Nanofluidics allows the analysis of small samples (meaning advances such as small samples in security situations and small blood samples in medical clinical usage) and also allows the use of small quantities of reagents and probe molecules, which often are extremely expensive. Also, compared with currently developed microfluidic systems, nanofluidic systems have more precise fluid control due to the smaller fluid volume involved. Therefore, it is more advantageous in the manipulation and separation of biomolecules at the nano-scale in the Nano-Total Analysis Systems (nTAS).

With the rapid development of nanotechnology in the past few decades, nanofluidic system fabrication has been realized through different types of fabrication technologies [**17**]. More and more research efforts have been put in this area due to its unique properties and advantages over microfluidic systems. However, there are key issues that must be addressed for the successful integration of nano-scale fluidic systems into sensing and chemical processing platforms. These are communicating with the "outside world" and developing the actual means of nanofluidic flow control. There is no avoiding the need to interface with the macro-world but, due to the extremely tiny volumes of nanofluidic systems (of the order of femto-liter), the interfacing can be the main bottleneck in further development for nanofluidics.

The general approach that has been taken in integrating nanofluidics into analytical and chemical processing systems is to have a nanofluidic channel in communication with a microfluidic channel which is, in turn, in communication with a fluid reservoir. With proper surface treatments, fluid in the reservoir wets and fills the

microfluidic channel and capillary action then allows this fluid to fill the nanofluidic channel. After the filling of the full fluidic system, flow can be established by one of the following three ways [**18**][**19**][**20**]: (1) electroosmosis, (2) electrophoresis, or (3) pressure gradients. Of these, pressure-driven flow is more general since it does not necessitate the presence of charged entities and therefore does not rely on the complexities of their motion.

The use of a direct, pump-imposed, pressure gradient across a nanofluidic channel has been tried (see Figure **2-4.a**) but tends to be unstable for the pumps commonly used and leads to excessive sample residence times in the series-connected microfluidic channel [**20**]. A different configuration using independent flow in each of the connecting microfluidic channels has been explored recently to produce a microfluidic channel flow-caused pressure gradient across a nanofluidic channel, as seen in Figure **2-4.b** [**21**]. This approach allows the residence times in the microfluidic channels to be independent of the pressure gradient across the nanofluidic channel, permitting very short residence times in the microfluidic channels. The up-stream reservoir and microfluidic channel, then the nanofluidic channel, and finally the down-stream microfluidic channel are sequentially filled to avoid air bubble problems in this configuration. However, the approach requires multiple syringe pumps and an extra back pressure control unit is needed resulting in system complexity. And measuring the actual nanofluidic flow rate relies on an indirect approach using fluorescence labeling, therefore, additional fluorescence optics.

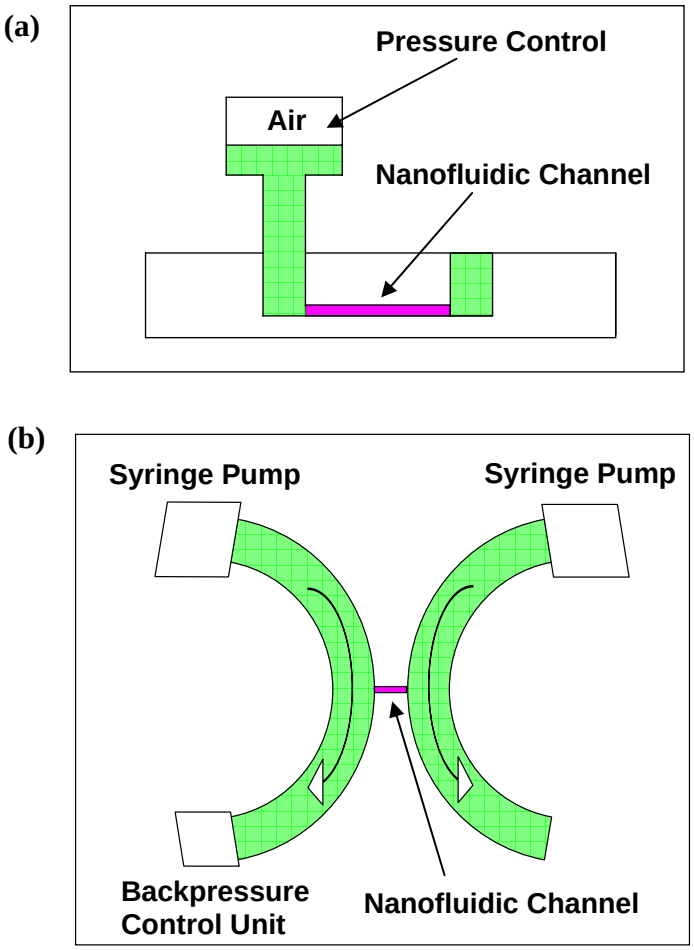

Figure **2-4**: (a) Schematic of nanofluidic flow control system (side view) using the approach of a direct, pump-imposed, pressure gradient across a nanofluidic channel, (b) schematic of a nanofluidic flow control system (top view) using the approach of flow in independent microfluidic channels causing a pressure gradient across a nanofluidic channel. In both (a) and (b) purple represents the nanofluidic channels and green represents the microfluidic channels.

In this work, we introduce a new approach to employing pressure-driven flow which is depicted in Figure **2-5**. We term this approach parallel flow control (PFC). PFC uses flow in a microfluidic flow control channel, which interfaces with the "outside world", to set up the pressure gradient across a nanofluidic channel and the residence

time in this microfluidic channel is established solely by its flow. PFC has two versions as seen in Figure **2-5.a** and Figure **2-5.b**: (1) one in which the pressure gradient across the nanofluidic channel is controlled by the microfluidic channel flow at points A and B and (2) another where it is controlled by the microfluidic channel flow and a fixed pressure at point B (e.g., point B is at atmospheric pressure). Air bubble avoidance is easily attained by first filling the up-stream reservoir and the microfluidic flow control channel in both versions.

The corresponding electric circuit model to our parallel flow control approach is shown in Figure **2-6.c**. The electric current through the larger resistor (R) is controlled by the current through the smaller resistor in parallel (r). Therefore, the nanofluidic channel flow rate (Q_n) can be controlled by the microfluidic flow control channel flow rate (Q_m).

As we will demonstrate later, the PFC approach of either version (1) (Figure **2-5.a**) or version (2) (Figure **2-5.b**) can provide essentially infinitely fine nanofluidic channel flow control by using one syringe pump, the most universal fluid handling instrument. While the flow rate through the microfluidic channel can be varied from 1 μl/hr to 1 l/hr in versions (1) and (2) by using a syringe pump, the flow rate through the nanofluidic channel can be adjusted by changing the dimensions of these two channel types. Based on the size-scale differences between nano- and micro-fluidic channels, flow rate ratios of 10^{-4}:1 and smaller values are easily attainable with the PFC approach thereby allowing the attainment of a broad range of fine nanofluidic flow rate control.

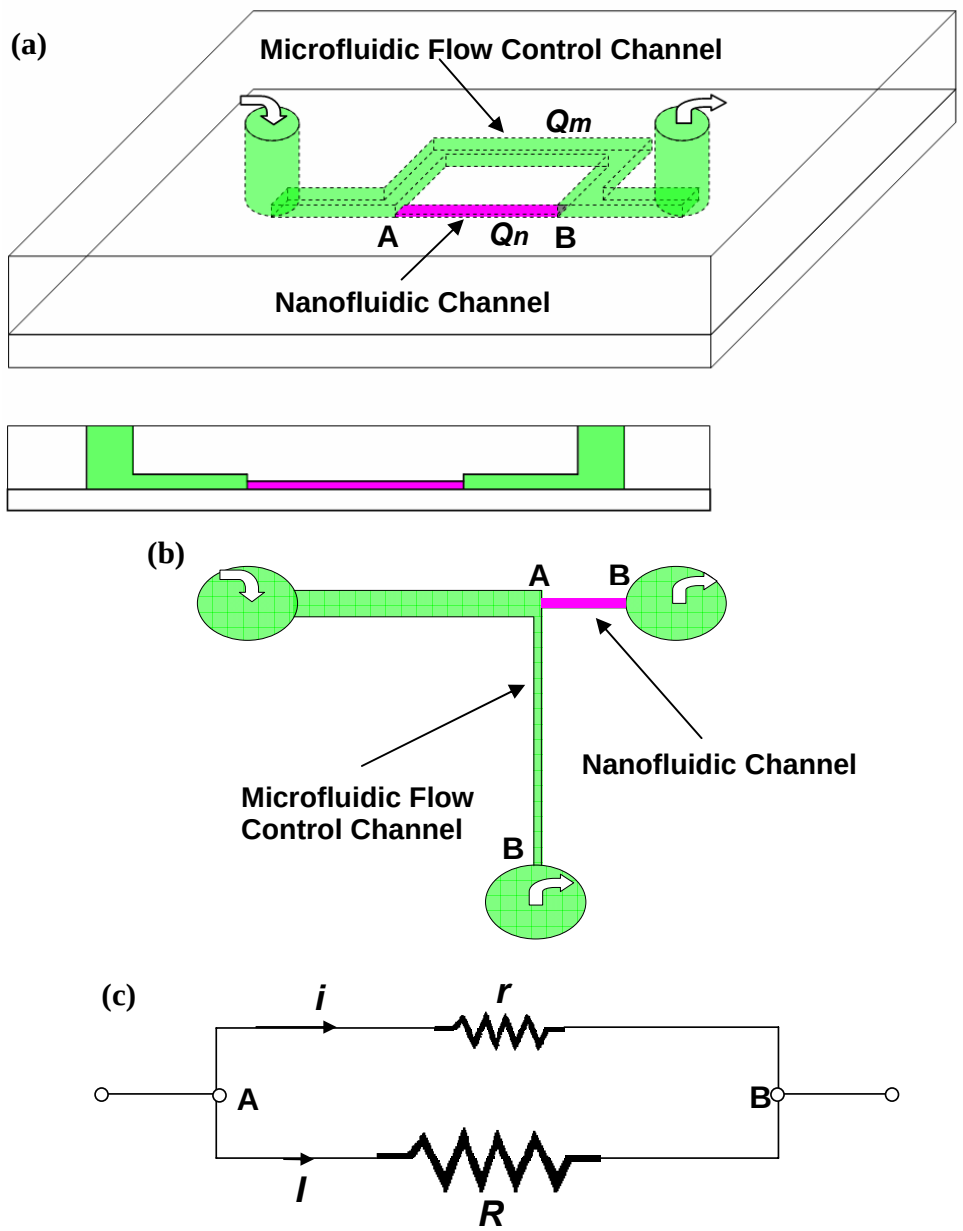

Figure **2-5**: Schematics of the parallel flow control (PFC) approach for nanofluidic flow control. (a) Version (1) where the pressure gradient across the nanofluidic channel is controlled by the microfluidic flow at points A and B (top and side views), (b) version (2) where the pressure gradient is controlled by the microfluidic flow at A and by a fixed pressure (e.g., atmospheric pressure) at B (top view). In the schematics, the purple represents the nanofluidic channels and green represents the microfluidic channels. (c) The corresponding electric circuit model. *R* and *r* represent the flow resistance of nanofluidic channel and microfluidic channel, respectively.

2.2.1 Theoretical Analysis

We have established our assessment of the flow rate ratios available using PFC by using the simple fluidic flow model sketched in Figure **2-6**.

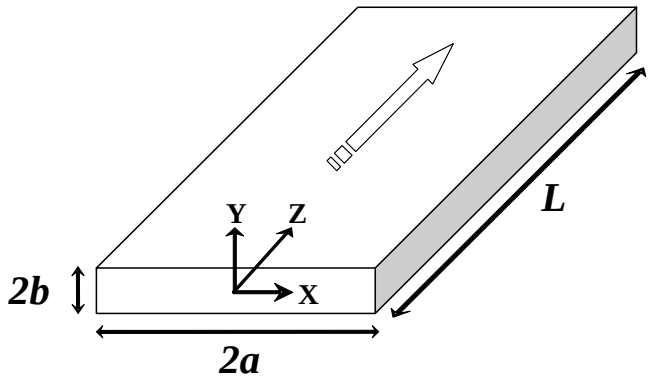

Figure **2-6**: The schematic of fluidic flow model. Here 2*a*, 2*b* and *L* are channel width, height and length respectively.

Assuming a single one phase Newtonian flow in the channel shown above and a pressure gradient $-dp/dz$ along the flow direction, it follows from mass conservation and momentum conservation that the velocity field $u(x,y)$ of fully developed flow can be written as [**22**]

$$u(x,y)=\frac{16b^2}{\eta\pi^3}\left(-\frac{dp}{dz}\right)\sum_{n=1,3,5,\ldots}^{\infty}(-1)^{(n-1)/2}\left[1-\frac{\cosh(n\pi x/2b)}{\cosh(n\pi a/2b)}\right]\frac{\cos(n\pi y/2b)}{n^3} \qquad \textbf{2.2}$$

where η is viscosity and the other parameters are defined in Figure **2-6**. The total flow rate Q deduced from this equation is

$$Q = \int_{-a}^{a}\int_{-b}^{b} u(x,y)dxdy$$
$$= \frac{128b^3}{\eta\pi^4}\left(-\frac{dp}{dz}\right)\sum_{n=1,3,5,\ldots}^{\infty}\left[a - \frac{2b}{n\pi}\tanh(n\pi a/2b)\right]\frac{1}{n^4} \qquad \textbf{2.3}$$

Neglecting any entry effects, we take the pressure gradient to be constant through the whole channel, whether it is a nanofluidic channel or microfluidic channel. Hence, we have

$$-\frac{dp}{dz} \approx \frac{\Delta p}{L} \qquad \textbf{2.4}$$

where Δp is the pressure drop along a given channel from point A to B and L is the channel length from point A to B. In both versions of the PFC approach the nanofluidic and microfluidic channels are in parallel with the length L_n for the nanofluidic channel and the length L_m for the microfluidic channel. Therefore, using Eq. **2.4** we can now write the flow rate ratio Q_n/Q_m for nanofluidic channel flow to microfluidic channel flow in both PFC versions of Figure **2-5**. This ratio is

$$\frac{Q_n}{Q_m} = \frac{b_n^3\sum_{n=1,3,5,\ldots}^{\infty}\left[a_n - \frac{2b_n}{n\pi}\tanh(n\pi a_n/2b_n)\right]\frac{L_m}{n^4}}{b_m^3\sum_{n=1,3,5,\ldots}^{\infty}\left[a_m - \frac{2b_m}{n\pi}\tanh(n\pi a_m/2b_m)\right]\frac{L_n}{n^4}} \qquad \textbf{2.5}$$

Eq. **2.5** can be re-written as

$$\frac{Q_n}{Q_m} = \frac{C_n L_m}{C_m L_n} \qquad \textbf{2.6}$$

where C_n and C_m are seen from Eq. **2.5** to be geometric factors, for the nano- and micro-fluidic channels, respectively. These geometric factors have been discussed previously [**23**], which can be computed numerically in general. For the case where the channel height is much smaller than channel width ($2b<<2a$), as a result, the flow through the channel is simplified to what is termed the plane Poiseuille flow/Hele Shaw flow, and the ratio C_n/C_m can be simply expressed as $a_n b_n^3 / a_m b_m^3$ [**22**]. Since $2b<<2a$ is very valid for our nanofluidic channels and approximately true for some of the microfluidic channels we used, we are often able to evaluate Eq. **2.6** using

$$\frac{Q_n}{Q_m} = \frac{a_n b_n^3 L_m}{a_m b_m^3 L_n} \qquad \textbf{2.7}$$

For a 100 nm high nanofluidic channel and a 2 μm high microfluidic channel connected in parallel with same width and length scale, the flow rate ratio is 1.25×10^{-4}:1. In any case, we can see from Eq. **2.6** that the microfluidic flow control channel flow rate can be used to control a very precise (fine) flow through the nanofluidic channel in parallel.

References

1. D.C. Harris, *Quantitative Chemical Analysis*. W.H. Freeman and Company, New York, NY (1999)

2. H.L.F. von Helmholtz, "Ueber einige Gezetze der Verteilung elektrischer Strome in Korperliche Leitern mit Anwendung auf die Thierisch-Electrischen Versuche," *Ann. Physik* **89:** 211-233, (1853)

3. H.L.F. von Helmholtz, "Studien Uber Electrische Grenzschichten," *Ann. Physik* **7:** 337-382, (1879)

4. G. Gouy, "Sur la Constitution de la Charge Electrique a la Surface dun Electrolyte," *J. Phys. Radium* **9:** 457-468 (1910)

5. D.L. Chapman, "A Contribution to the Theory of Electrocapillarity," *Phil. Mag.* **25:** 475-481 (1913)

6. O. Stern, "Zur Theore der Elektrischen Doppelschicht," *Z. Elektrochemj.* **30:** 508-516, (1924)

7. D. Figeys, and D. Pinto, "Lab-on-a-Chip: A revolution in Biological and Medical Sciences," *Analytical Chemistry* **72:** 330-335, (2000)

8. K.K. Jain, "Lab-on-a-Chip and Microarrays: Discovery and Development," *Pharmacogenomics* **4:** 123-125, (2003)

9. R.C. Anderson, G.J. Bogdan, Z. Barniv, T.D. Dawes, J. Winkler, and K. Roy, "Microfluidic Biochemical Analysis System," *Proceedings of International Conference on Solid-State Sensors and Actuators* **1:** 477-480, (1997)

10. E.M.J. Verpoorte, B.H. Van Der Schoot, S. Jeanneret, A. Manz, H.M. Widmer, and N.F. De Rooij, "Three-dimensional Micro Flow Manifolds for Miniaturized Chemical Analysis Systems," *Journal of Micromechanics and Microengineering* **4:** 248-256, (1994)

11. M. Tokeshi, T. Minagawa, K. Uchiyama, A. Hibara, K. Sato, H. Hisamoto, and T. Kitamori, "Continuous-flow Chemical Processing on a Microchip by Combining Microunit Operations and a Multiphase Flow Network," *Analytical Chemistry* **74:** 1565-1571, (2002)

12. J.O. Tegenfeldt, C. Prinz, H. Cao, R.L. Huang, R.H. Austin, S.Y. Chou, E.C. Cox, and J.C. Sturm, "Micro- and Nanofluidics for DNA Analysis," *Analytical and Bioanalytical Chemistry* **378:** 1678-1692, (2004)

13. J.T. Mannion, and H.G. Craighead, "Nanofluidic Structures for Single Biomolecule Fluorescent Detection," *Biopolymers* **85:** 131-143, (2007)

14. G.O.F. Parikesit, V.G. Kutchoukov, W. Van Oel, G.L. Lung, A. Bossche, I.T. Young, and Y. Garini, "Optical Detection of Single Molecules in Nanofluidic Chips," *Proceedings of The International Society for Optical Engineering* **5515:** 109-116, (2004)

15. M. Foquet, J. Korlach, W. Zipfel, W.W. Webb, and H.G. Craighead, "DNA Fragment Sizing by Single Molecule Detection in Submicrometer-sized Closed Fluidic Channels," *Analytical Chemistry* **74:** 1415-1422, (2002)

16. J. Seokwoo, V. Malyarchuk, J.O. White, and J.A. Rogere, "Optically Fabricated Three Dimensional Nanofluidic Mixers for Microfluidic Devices," *Nano Letters* **7:** 1351-1356, (2005)

17. J.L. Perry, and S.G. Kandlikar, "Review of Fabrication of Nanochannels for Single Phase Liquid Flow," *Microfluidics and Nanofluidics* **2:** 185-193, (2006)

18. T.S. Hug, N.F. Rooij, and U. Staufer, "Fabrication and Electroosmotic Flow Measurements in Micro- and Nanofluidic Channels," *Microfluid Nanofluid* **2:** 117-124, (2006)

19. Y. Chen, A. Pepin, P. Youinou, V. Studer, and A. Lebib, "Nanoimprint Lithography for the Fabrication of DNA Electrophoresis Chips," *Microelectronic Engineering* **61:** 927-932, (2002)

20. F.H.J. Van Der Heyden, D. Stein, and C. Dekker, "Streaming Currents in a Single Nanofluidic Channel," *Physical Review Letters* **95:** 116104, (2005)

21. E. Tamaki, A. Hibara, H.B. Kim, M. Tokeshi, and T. Kitamori, "Pressure-driven Flow Control System for Nanofluidic Chemical Process," *Journal of Chromatography A* **1137:** 256-262, (2006)

22. J.P. Brody, P. Yager, R.E. Goldstein, and R.H. Austin, "Biotechnology at Low Reynolds Numbers," *Biophysical Journal* **71:** 3430-3441, (1996)

23. M. Richter, P. Woias, and D. Wei, "Robust Design of Gas and Liquid Micropumps," *Sensors and Actuators A* **62:** 480-483, (1997)

Chapter 3

Parallel Flow Control (PFC) Device and Integrated Analytical System Fabrication

The fabrication procedure of all the related devices used in this study including individual parallel flow control devices and integrated analytical systems consisting of nano-gap sensing structure and nanofluidic flow control component is presented in this chapter. The individual parallel flow control device based on glass etching and bonding is utilized to demonstrate the novel nanofluidic flow control approach which will be applied to the integrated analytical system. The integrated analytical system fabrication consists of nano-gap sensing structure fabrication and PDMS based nanofluidic flow control component fabrication. Surface micromaching technology is used in all of the fabrication processes. By using this technology, which is adopted from the microfabrication technology developed in application specific integrated circuit (ASIC) applications, the highly parallel batch fabrication fashion to produce a large number of identical devices at a cost savings for an individual device can be achieved. To ensure the high device yield, the whole process is carried out in the Penn State Nanofabrication class-10 cleanroom facility.

3.1 Parallel Flow Control Device Fabrication

As discussed in Chapter 2, PFC uses flow in a microfluidic flow control channel, which interfaces with the “outside world”, to set up the pressure gradient across a

nanofluidic channel and the residence time in this microfluidic channel is established solely by its flow.

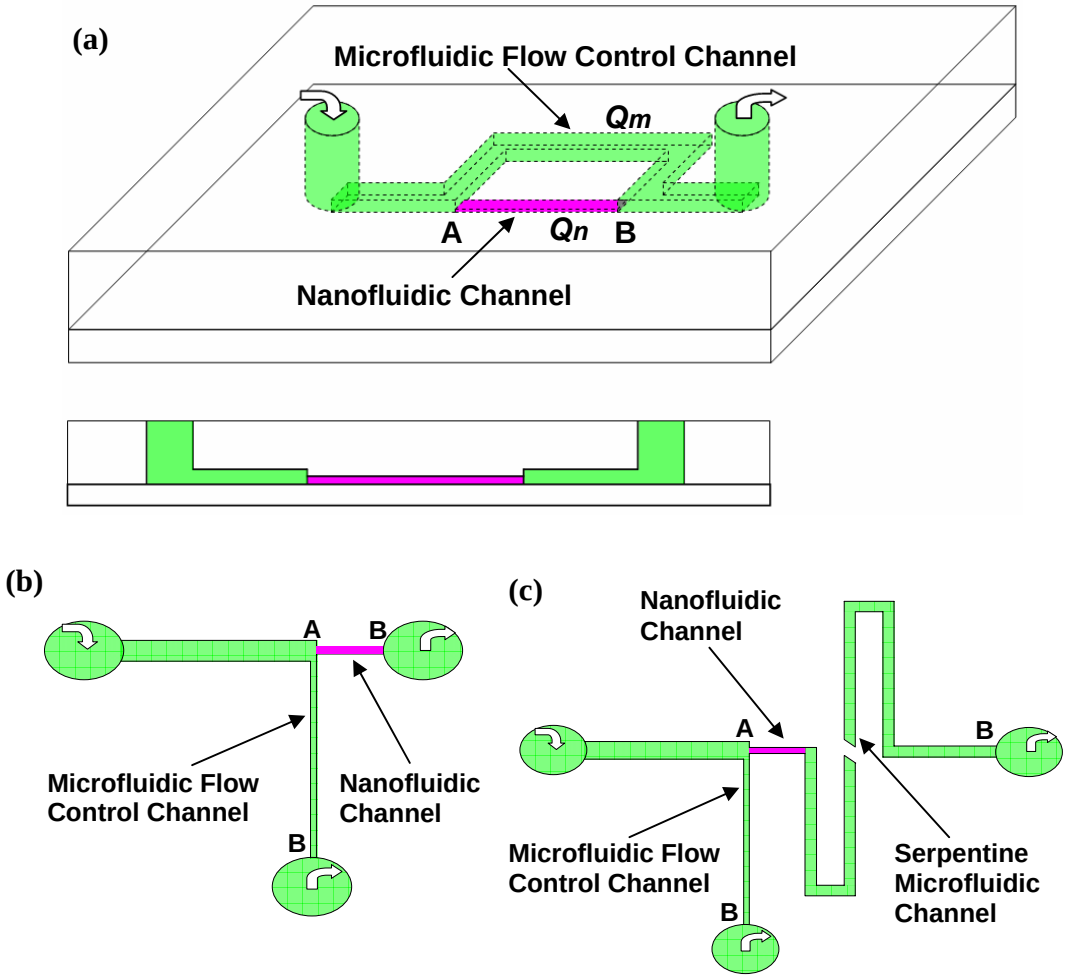

Figure **3-1**: Schematics of the parallel flow control (PFC) approach for nanofluidic flow control. (a) Version (1) where the pressure gradient across the nanofluidic channel is controlled by the microfluidic flow at points A and B (top and side views), (b) version (2) where the pressure gradient across the nanofluidic channel is controlled by the microfluidic flow at A and by a fixed pressure (e.g., atmospheric pressure) at B (top view), (c) version (2) with an additional serpentine microfluidic channel designed to measure the flow through the nanofluidic channel. In the schematics, purple represents the nanofluidic channels and green represents the microfluidic channels.

PFC has two versions as seen in Figure **3-1.a** and Figure **3-1.b**: (1) one in which the pressure gradient across the nanofluidic channel is controlled by the microfluidic channel flow at points A and B and (2) another where it is controlled by the microfluidic channel flow and a fixed pressure at point B (e.g., point B is at atmospheric pressure). Similar flow control structure of version (1) will be utilized to integrate with nano-gap sensing structure to construct final biomolecule detection system.

The fabrication processes of the devices used in our demonstration and preliminary evaluation of the PFC concept are CMOS compatible allowing potential application in future integrated Micro-/Nano-Total Analysis Systems. The overall fabrication processes for version (1) are shown in Figure **3-2**. First of all, glass slides (Fisherbrand plain glass microslides) are prepared with standard RCA cleaning (SC1&SC2) process, followed by DI water rinsing, and then a 150 ^{o}C baking for 10 minutes. As seen, the nanofluidic channel (100 nm high, 16 μm wide, and 200 μm long) is first dry etched into a glass slide in a magnetically enhanced reactive ion etching (MERIE) tool using photoresist SPR 3012 as the etching mask. The optical lithography and dry etching parameters are listed in Table **3-1** and Table **3-2** respectively. Then the microfluidic flow control channel (2 μm high, 20 μm wide, and 400 μm long) is patterned in alignment with the nanofluidic channel using wet chemical etching (6:1 buffered oxide etch solution) with photoresist SPR 3012 as the etching mask. Before wet etching microfluidic channel, an oxygen plasma descuming step in a plasma reactor (M4L) is required to remove the photoresist residual film on the surface (50 sccm, 400 mTorr, and 100 W for 4 minutes). Subsequently, the reservoir/access ports are

mechanically drilled through the glass slide. Finally, the patterned glass slide is bonded with another blank glass slide in furnace at 615 ^{o}C for 1.5 hours to complete the sealed fluidic flow control devices.

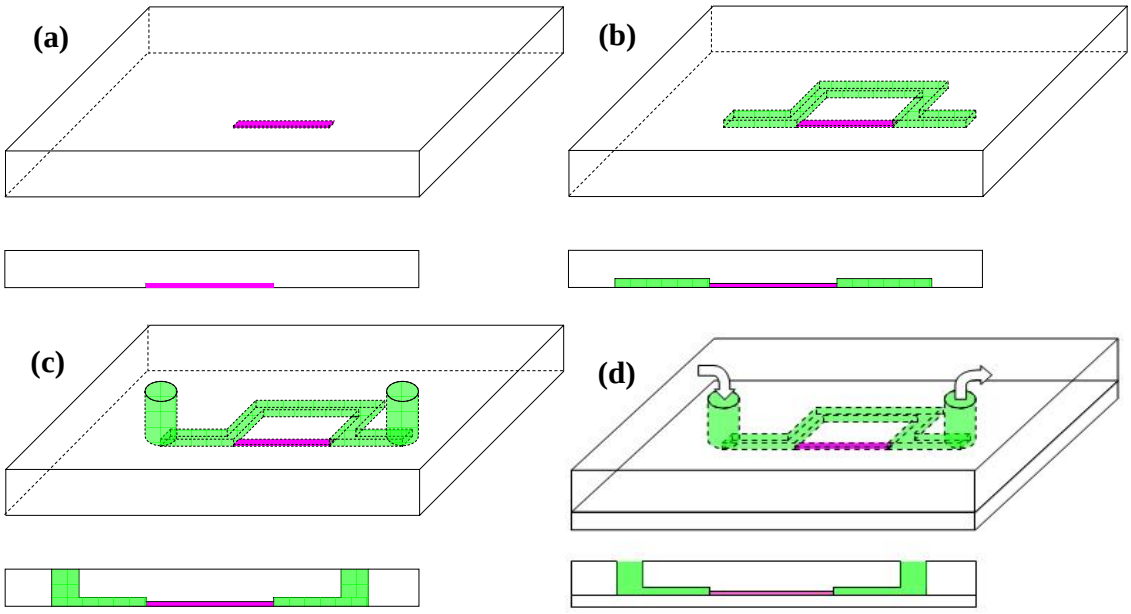

Figure **3-2**: (a) Nanofluidic channel patterned in glass by dry etching, (b) microfluidic flow control channel patterned in glass by wet etching, (c) access ports drilled through glass, (d) the schematic of the active nanofluidic flow control system after glass bonding. Top and cross-sectional views are shown in each case. Purple represents the nanofluidic channel and green represents the microfluidic flow control channel.

Table **3-1**: SPR 3012 optical lithography parameters.

1. Dynamically Spin SPR 3012	@500 rpm for 8 seconds with 4000 rpm/second @4000 rpm for 45 seconds with 4000 rpm/second
2. Soft bake	@110 ^{o}C, 60 seconds
3. Expose	4.5 second @12 W
4. Post expose bake	@110 ^{o}C, 30 seconds
5. Develop	1 minute plus 15 seconds with mild agitation
6. Rinse	3 times in DI water
7. Dry	Nitrogen gun
8. Hard Bake	@110 ^{o}C, 2 minutes

Table **3-2**: MERIE dry etching parameters.

Chamber Pressure	30 mTorr
CF_3	50 sccm
Ar	25 sccm
Magnetic Field	50 Gauss
Power	350 W
Etching Rate	~50 nm/min

The specific processing steps for version (1) PFC devices are seen in Figure **3-3**. Figure **3-3** shows an actual version (1) PFC device under optical microscopy after thermal glass bonding. Figure **3-4** is the FESEM pictures of the nanofluidic channel cross section showing the approximate channel dimensions of 72.95 nm high and 15.65 μm wide. The actual channel height is smaller than designed (100 nm) due to glass reflowing while thermal bonding at 615 ^{o}C.

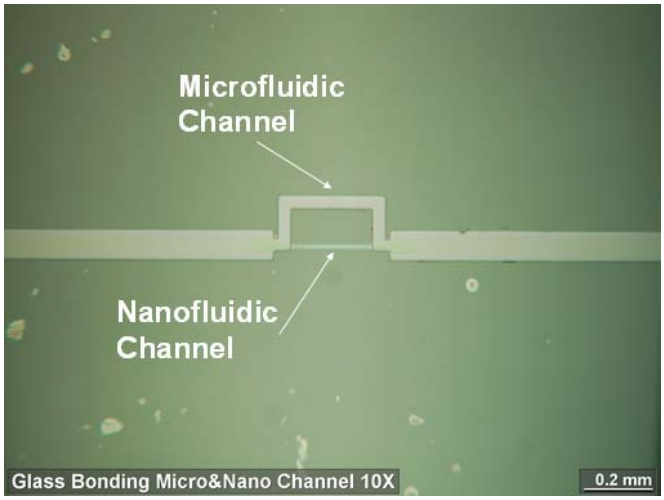

Figure **3-3**: Bonded nanofluidic flow control device as seen under optical microscopy.

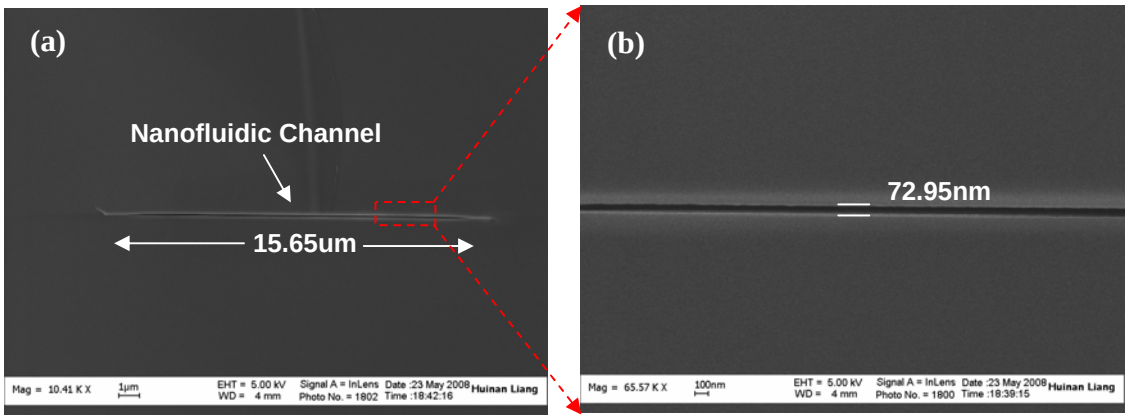

Figure **3-4**: (a) Cross-sectional FESEM picture of bonded nanofluidic channel, (b) exaggerated nanofluidic channel cross section for dimension clarity. The nanofluidic channel is about 72.95 nm high and 15.65 μm wide.

The fabrication for version (2) devices (Figure **3-1.c**) is carried out following the same basic processes illustrated in Figure **3-2**. The particular version (2) device to be discussed here is that of Figure **3-1.c**; i.e., it has a microfluidic flow control channel (10 μm high, 10 μm wide, and 4350 μm long) and an additional serpentine microfluidic channel (10 μm high, 20 μm wide, and 8 cm long) in series with the nanofluidic channel.

The actual device structure is seen in Figure **3-5**. The additional serpentine microfluidic channel is designed to allow the direct measurement of flow rate through the nanofluidic channel by tracking the water-air interface movement into the serpentine microfluidic channel. Figure **3-5.a** shows this flow rate measurement device under optical microscopy. Due to the scale difference, the pressure drop across the serpentine microfluidic channel length is negligible compared with the pressure drop across the

nanofluidic channel length. Therefore, our flow rate analysis in Chapter 2 is still valid for this configuration. Figure **3-5.b** shows the device with DI water infused into the system by a syringe pump. As seen, the water-air interface progression can be used to measure the filling rate of the serpentine microfluidic channel thereby measuring flow rate through the nanofluidic channel.

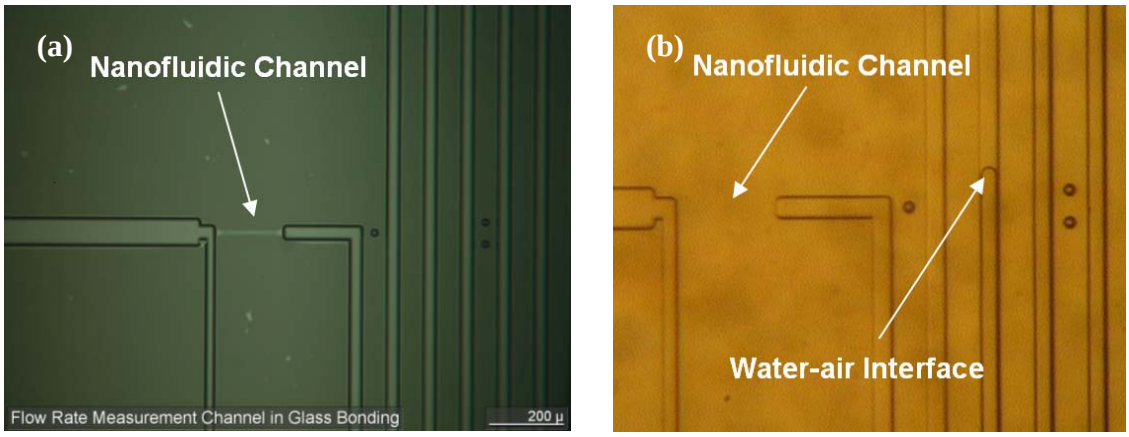

Figure **3-5**: Version (2) with an additional serpentine microfluidic channel in series with the nanofluidic channel. (a) Bonded nanofluidic flow rate measurement device under optical microscopy, (b) same device with water infused by a syringe pump and the water-air interface visible in the serpentine microfluidic channel.

In all of our flow demonstration and evaluation experiments, whether with the device types seen in Figure **3-3** or Figure **3-5**, needles are attached into the reservoir/access ports and connected to the fluidic source controlled by a syringe pump via plastic tubing.

3.2 Integrated Analytical System Fabrication

The integrated analytical system in this work consists of a sub-50 nm gap capacitor sensing structure and micro- and nano-fluidic control components. A schematic system setup is shown in Figure **3-6**.

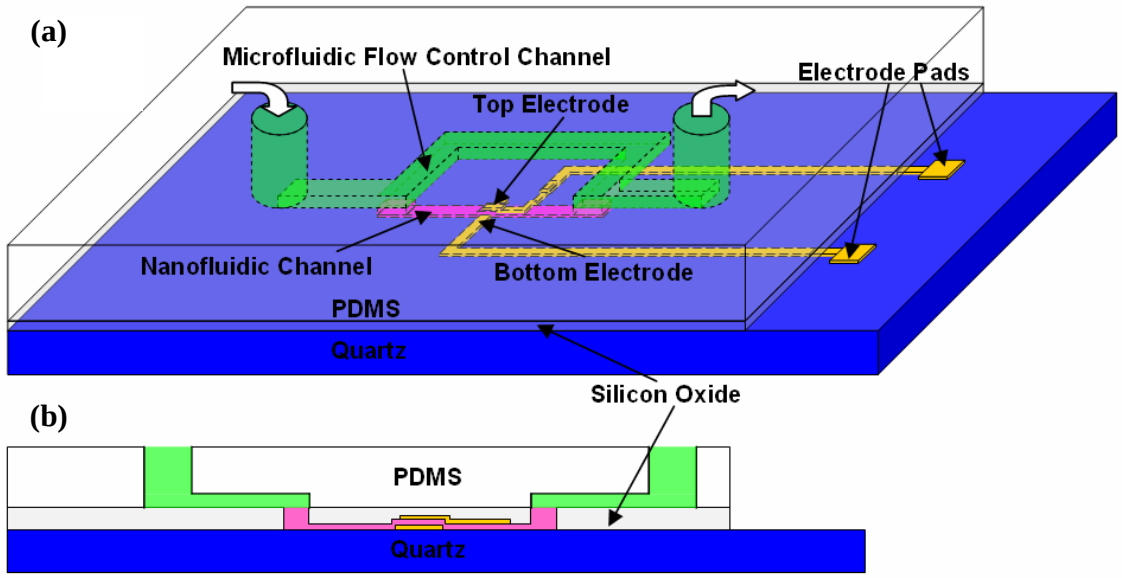

Figure **3-6**: The schematic of the nano-gap biomolecular sensor: (a) top view and (b) cross-sectional view. Green path represents microfluidic flow in PDMS, and purple represents nanofluidic flow through the nano-gap sensing structure.

The nano-gap capacitor sensing structure is constructed on 1 mm thick, two-side polished quartz wafers commercially available from Silicon Quest International, Inc. The nano-gap capacitor sensing structure, in its metal electrode version, is fabricated with three consecutive metal evaporations followed by 10 μm thick ECR-PECVD (electron cyclotron resonance plasma enhanced chemical vapor deposition) oxide deposition, patterning, and sacrificial metal etching. In the integrated analytical system, unlike the

previous individual flow control devices based on glass etching, the microfluidic flow control channel is fabricated in PDMS by using soft lithography, and is bonded with nan-gap capacitor sensing structure to produce a self-contained intact analytical system. The microfluidic flow control channel in PDMS will act as the interface to external fluidic system by connecting with a syringe pump via plastic tubing. As described earlier, the microfluidic flow control channel will also be used to control the flow through the nanofluidic channel feeding the nano-gap sensing structure. The exposed electrode pads seen in Figure **3-6** are then connected with an Agilent 4284A LCR meter for electrical signal acquisition and processing.

3.2.1 Nano-Gap Sensing Device Fabrication

3.2.1.1 Substrate Preparation

Related research by others has shown the extreme importance of the electrical properties of device substrates [**1**]. Therefore, 1 mm thick, two-side polished quartz wafers are used in this work due to their excellent insulation properties. By using quartz wafers, the background noise from parasitic capacitance will be further minimized. These quartz wafers are prepared with standard RCA cleaning (SC1&SC2) process, followed by DI water rinsing, and then a 150 ^{o}C baking for 10 minutes.

3.2.1.2 Three Layers of Metal Evaporation

A lift-off process is used to pattern all the metal layers on the device to ensure the accurate topographic control. Figure **3-7** shows the schematic of the typical lift-off process used. Lift off resist (LOR) is used to avoid the rabbit ears which can interfere with the lift-off process [**2**].

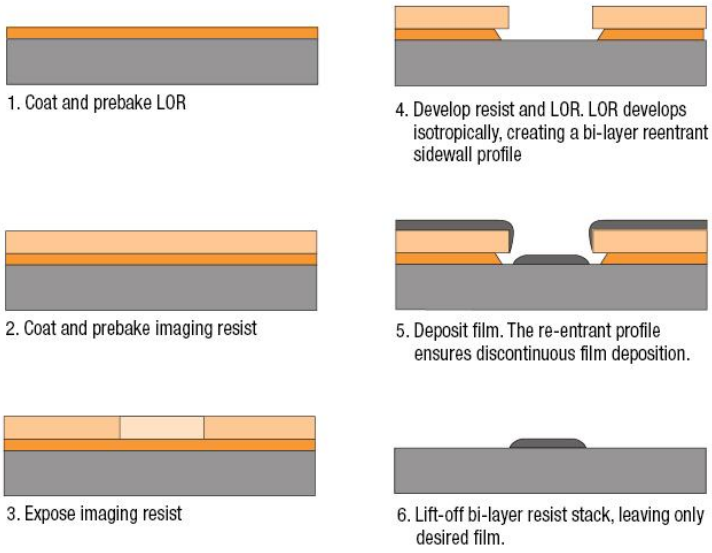

Figure **3-7**: The schematic of lift-off process [**2**].

In this lift-off part of the work, SPR 3012 positive photoresist and LOR 5A are used. The optical lithography process parameter is listed in Table **3-3**. Before loading the samples into an evaporation chamber, a 10-20 second oxygen plasma descuming (Ar 5 sccm, O_2 40 sccm, 100 mTorr, and 100 W) in DRIE system (PT 720) is performed to etch away the organic film residue left on the exposed area from the photolithography process.

This step is extremely important for following metal evaporation to improve the metal adhesion with substrate by providing a perfectly clean interface.

Table **3-3**: Lift off process optical lithography parameters.

1. Dynamically Spin LOR 5A	@500 rpm for 8 seconds with 4000 rpm/second @4000 rpm for 50 seconds with 4000 rpm/second
2. Soft bake	@175 ^{o}C, 5 minutes
3. Dynamically Spin SPR 3012	@500 rpm for 8 seconds with 4000 rpm/second @4000 rpm for 45 seconds with 4000 rpm/second
4. Soft bake	@110 ^{o}C, 60 seconds
5. Expose	4.5 second @12 W
6. Post expose bake	@110 ^{o}C, 30 seconds
7. Develop	1 minute plus 15 seconds with mild agitation
8. Rinse	3 times in DI water
9. Dry	Nitrogen gun

The three layers of metal evaporation consist of the bottom layer of gold (25 nm Au with 5 nm Ti as adhesion layer) which functions as the bottom electrode, a middle layer of nickel (50 nm Ni) which functions as a sacrificial layer, and a top layer of gold (45 nm Au with 5nm Ti on the top to improve the adhesion between top electrode and capping layer of oxide in the next step) which functions as the top electrode. The middle sacrificial layer of nickel will be wet chemically etched away after capping layer of oxide deposition and patterning, which yields a sealed nanofluidic channel structure between the bottom and top gold electrodes. Figure **3-8** shows the metal patterning processes in detail.

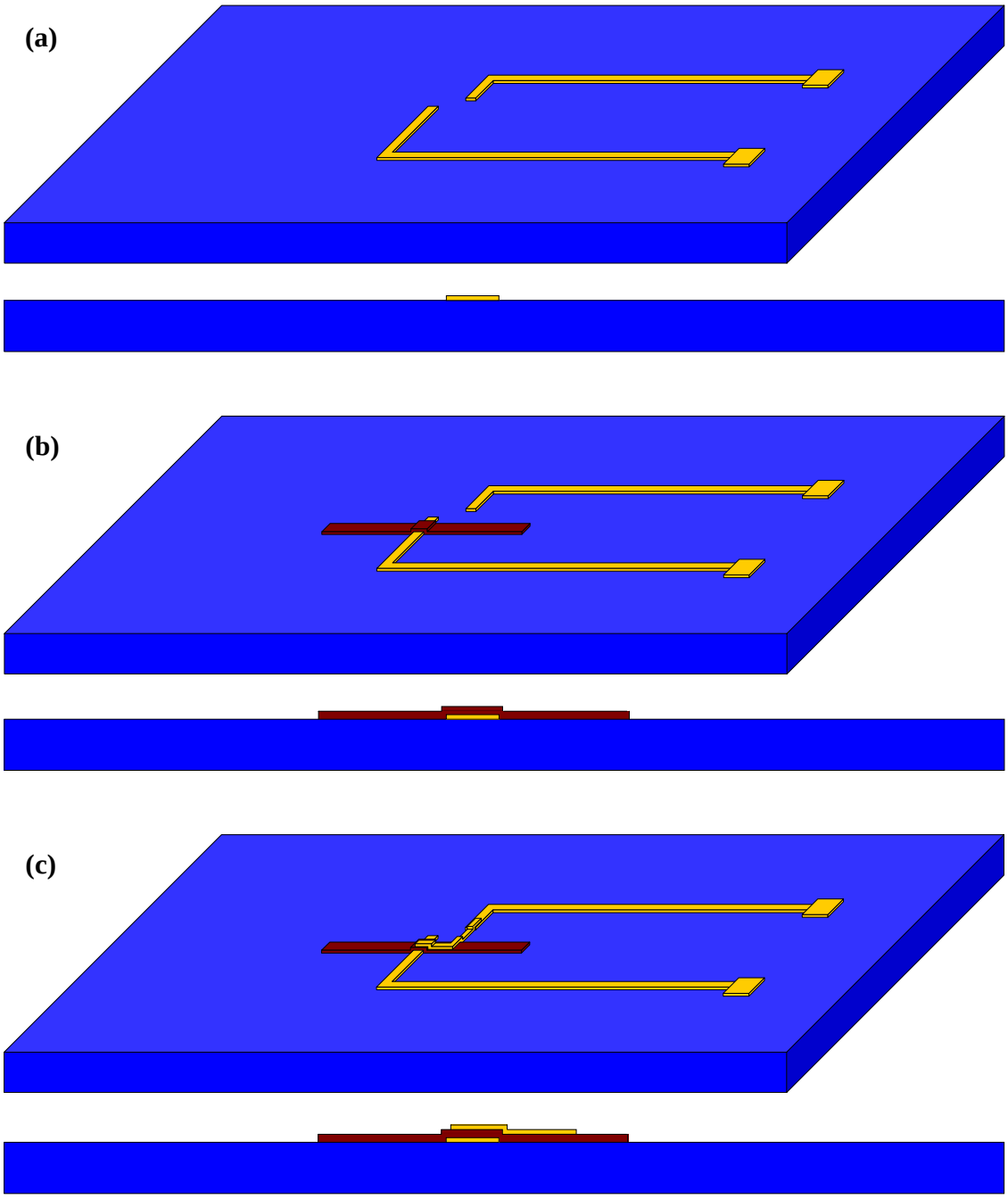

Figure **3-8**: (a) Bottom electrode (Au) patterning, (b) sacrificial layer (Ni) patterning, (c) top electrode (Au) patterning. Top view (top) and cross-sectional view (bottom) are shown in each case.

3.2.1.3 Capping Layer Deposition and Patterning

After the three layers of metal evaporation, a 10 μm thick low temperature oxide is deposited on the top in electron cyclotron resonance (ECR) plasma enhanced chemical vapor deposition (PECVD) tool. To improve the adhesion between this oxide and the substrate, the whole device is heated on hot plate at 150 ^{o}C for 10 minutes before being loaded into the ECR-PECVD chamber. The deposition parameters used are listed in Table **3-4** which is crucial to result in good quality thick oxide film with low built-in stress. Then SPR 3012 photoresist is patterned on the top to define two access ports (Table **3-1**). After an oxygen plasma descuming step, a 10:1 HF solution (49%) is used to etch two access ports in the deposited oxide to expose the middle sacrificial layer of nickel underneath. Finally, the middle sacrificial layer of nickel is wet chemically etched away (Transene Nickel Etchant Type 1) for 30 minutes at 70 ^{o}C on hot plate (Figure **3-9**). This completes the nano-gap sensing structure fabrication.

Table **3-4**: Low temperature oxide deposition parameters.

Pressure	4 mTorr
Ar Flow Rate	3 sccm
O Flow Rate	5.1 sccm
SiH Flow Rate	4 sccm
RF2 Power	900 W

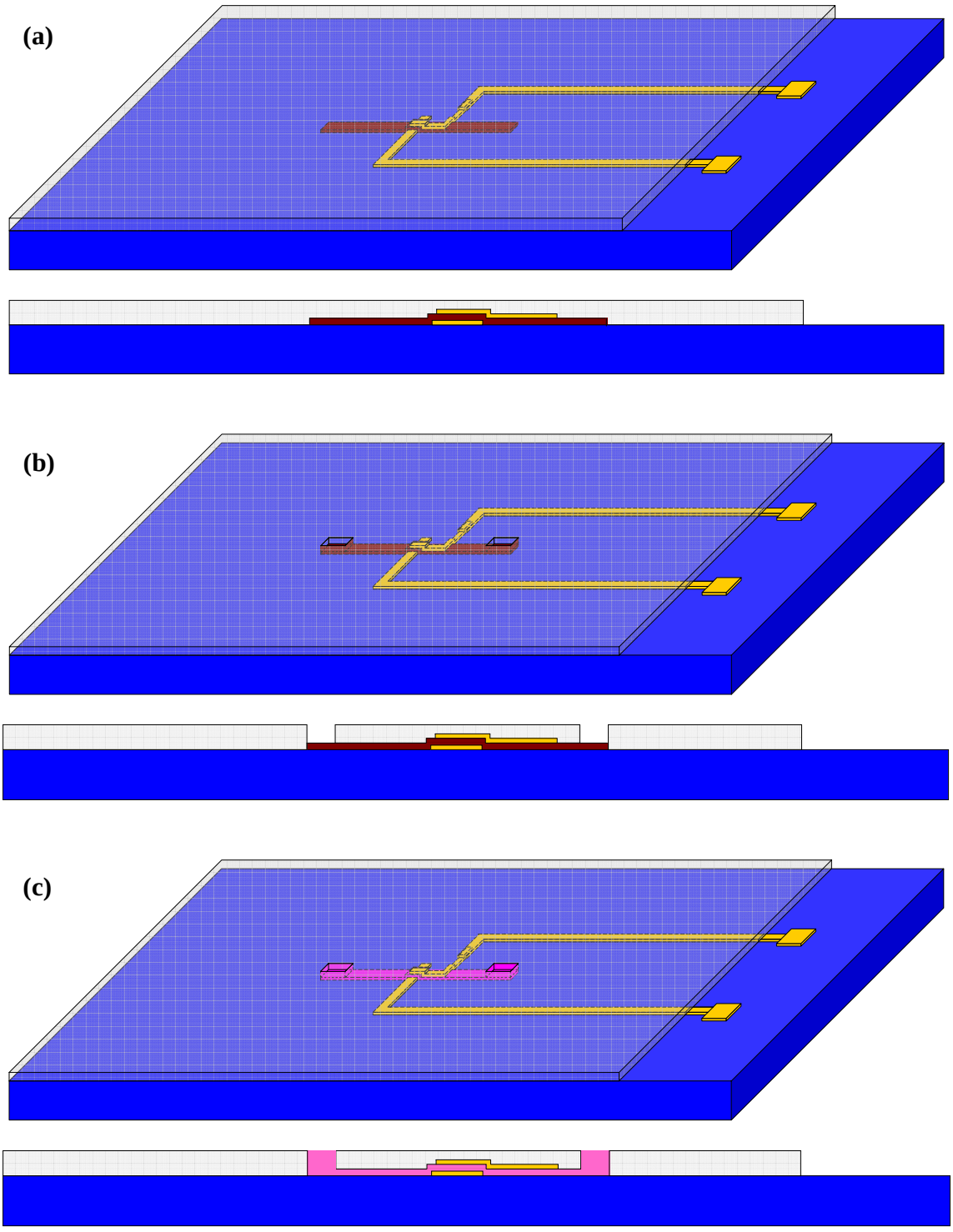

Figure **3-9**: (a) Low temperature oxide deposition, (b) access ports etching, (c) sacrificial layer (Ni) etching. Top view (top) and cross-sectional view (bottom) are shown in each case.

3.2.2 Microfluidic Flow Control Channel Fabrication

The microfluidic flow control channel of the integrated analytical system is fabricated in PDMS using soft lithography microfabrication technology. Unlike common photolithography where the device is fabricated on the substrate, soft lithography first makes a negative master mold using photolithography, and then transfers the pattern to the PDMS by casting an elastomeric material on the mold, curing it and peeling it off from the master mold. Generally, negative photoresist SU8 is used as the master mold material (Table **3-5**).

Table **3-5**: SU8-50 optical lithography parameters.

1. Dynamically Spin SU8-50	@500 rpm for 10 seconds with 100 rpm/second @3750 rpm for 30 seconds with 300 rpm/second
2. Soft bake	@65 ^{o}C, 5 minutes @95 ^{o}C, 10 minutes
3. Expose	10 seconds @12W
4. Post Expose Bake	@55 ^{o}C, 10 minutes @95 ^{o}C, 15 minutes
5. Develop	9-10 minutes with tiny agitation
6. Rinse	20 Seconds in IPA
7. Dry	Nitrogen gun

The superb thermal and chemical resistance of photoresist SU8 indicates the master mold can be used repeatedly. PDMS is an optically transparent and flexible silicone elastomer. Before using, PDMS pre-polymer and curing agents are mixed at a ratio of 10:1. The mixture can be completely cured at 65 ^{o}C for times such as two hours. After being cured, the patterned PDMS can be peeled off from the SU8 master mold, and can be bonded with a different substrate to produce a sealed structure with proper surface activation in oxygen plasma [**3**]. The whole process is shown in Figure **3-10**.

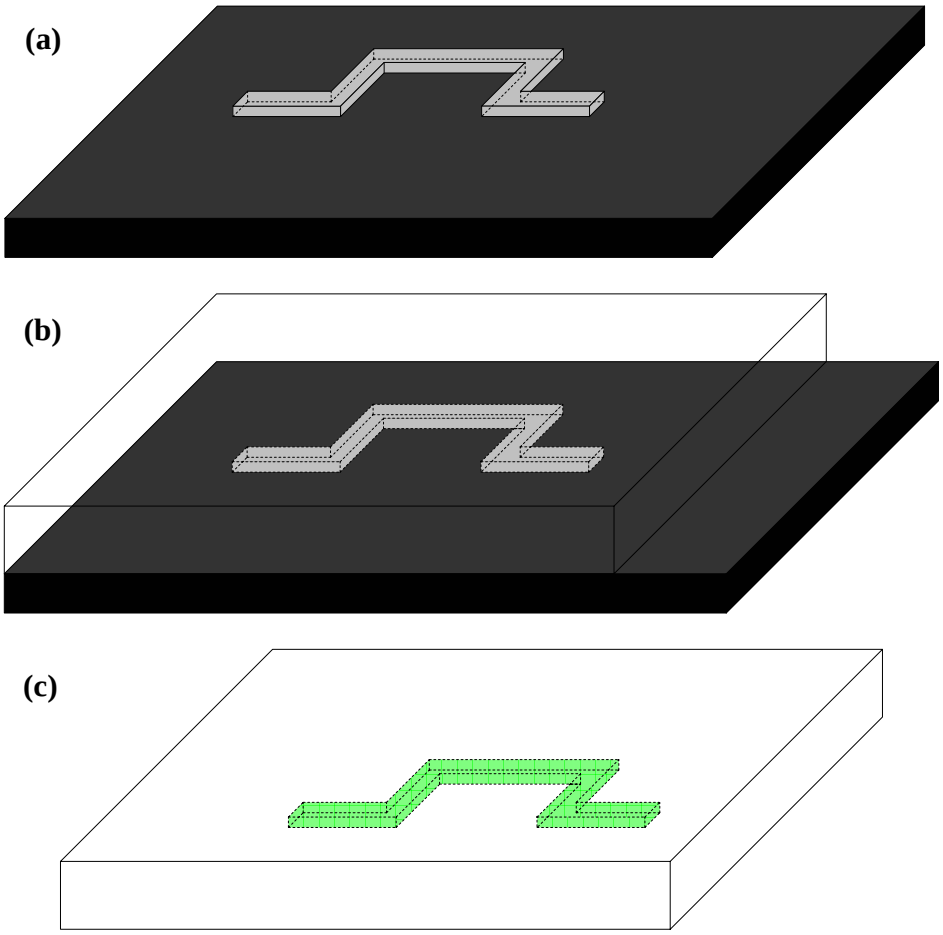

Figure **3-10**: (a) SU8 master mold patterning on substrate, (b) casting PDMS on the mold, (c) peeling off PDMS from the SU8 master mold after curing.

3.2.3 PDMS Bonding

After the PDMS is cured, it is peeled off from the master mold (Figure **3-10.c**) and two holes for input and output ports are drilled through it (Figure **3-12.a**). For bonding with the silicon oxide surface of the nano-gap sensing structure, super cleaning and proper activating is required for PDMS surfaces. PDMS is cleaned with acetone and

IPA, and then it is put in methanol for 10 minutes. After drying with nitrogen air, it is then loaded in a plasma reactor (M4L) to activate the surface at plasma power of 50 W, oxygen flow rate of 50 sccm, and chamber pressure of 400 mTorr for 20 seconds. The surface of PDMS needs to be properly activated and rendered hydrophilic with hydroxyl for bonding to the silicon oxide substrate via covalent bond [**4**]. Over activating will cause enhanced roughness of the surface which will prevent the bonding to the substrate. After the activation step, overnight bonding with the fabricated nano-gap sensing structure is done at room temperature to finish the integrated system fabrication (Figure **3-12.b**).

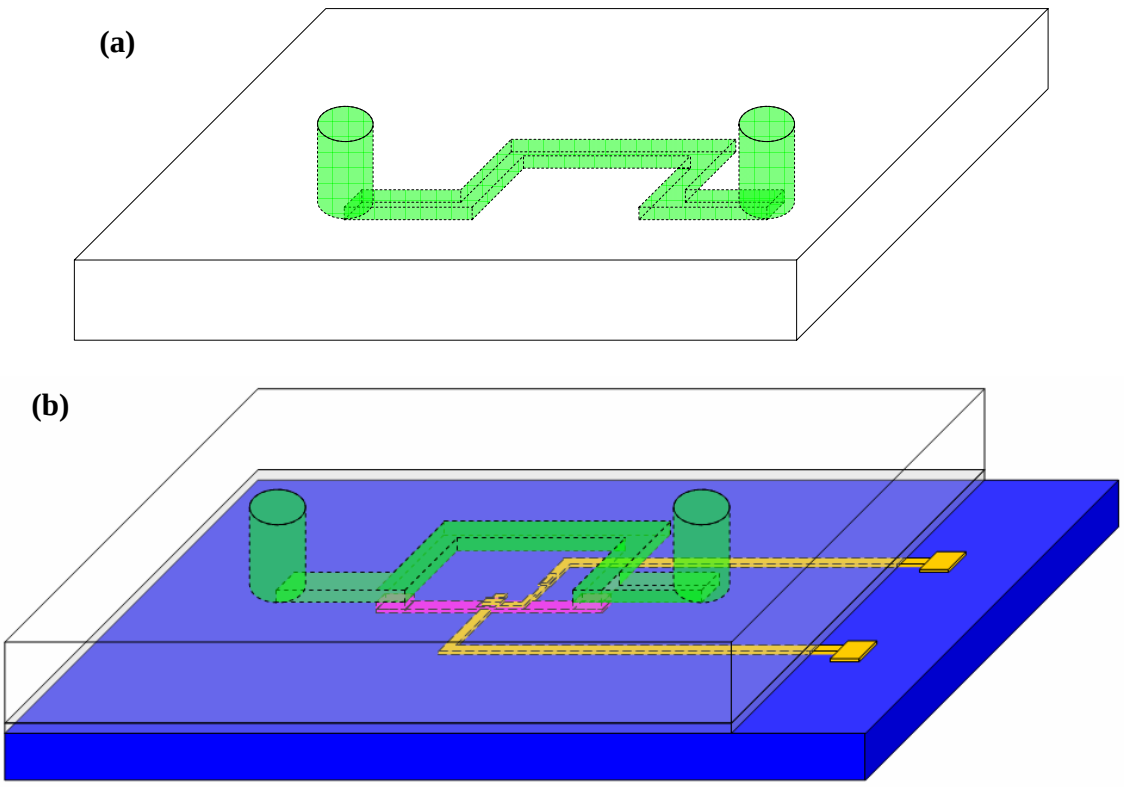

Figure **3-11**: (a) Two access ports drilled in PDMS, (b) PDMS bonded with nano-gap sensing structure e after oxygen plasma activating.

The actual completed integrated analytical system is shown in Figure **3-12** with arrow indicating the flow direction. There are totally 12 single nano-gap sensing devices on one single chip.

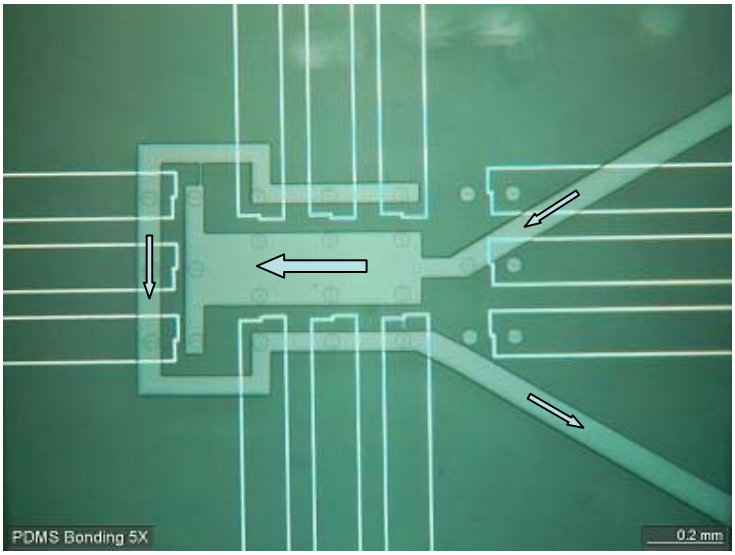

Figure **3-12**: Integrated system under optical microscopy after PDMS bonding with 12 single electrical sensing structures underneath.

References

1. J.W. Severinghaus, and P.B. Astrup, "History of Blood Gas Analysis. IV. Leland Clark's Oxygen Electrode," *Journal of Clinical Monitoring and Computing* **2:** 125-139, (1986)

2. MicroChem Corp. www.microchem.com

3. B.H. Jo, L.M. Van Lerberghe, K.M. Motsegood, and D.J. Beebe, "Three-dimensional Micro-channel Fabrication in Polydimethylsiloxane (PDMS) Elastomer," *Journal of Microelectromechanical System* **9:** 76-81, (2000)

4. S. Bhattacharya, a. data, J.M. Berg, and S. Gangopadhyay, "Studies on Surface Wettability of Poly(Dimethyl) siloxane (PDMS) and Glass Under Oxygen-plasma Treatment and Correlation with Bond Strength," *Journal of Microelectromechanical System* **4:** 590-597, (2005)

Chapter 4

Nanofluidic Parallel Flow Control Evaluation

In this chapter, the feasibility of parallel flow control approach to be utilized in our biomolecule detection system is demonstrated by using the individual nanofluidic flow control devices based on glass etching and bonding (version (1) and version (2)). The parallel flow control approach has been shown able to accomplish very fine nanofluidic flow control and measure the nanofluidic flow rate exceeding the current lowest limit reported in literature.

4.1 Optical Fluorescence Characterization

The fabrication and operation of the PFC concept is first evaluated using version (1). This evaluation is undertaken using optical fluorescence microscopy by infusing an Alexa Fluor fluorescein solution into the version (1) microfluidic flow control channel with a syringe pump (Figure **4-1.a**). Considering the nano-scale gap of our flow control device, it is clear that only minute amount of fluorescein molecules are available to be excited. To use fluorescence to examine our structure, a saturated fluorescein solution is utilized to increase the emitted light intensity and detectability. As seen, this results in the clear presence of fluorescein molecules in the nanofluidic channel. These fluorescein molecules can be removed by infusing DI water through the device for 5 minutes showing the ability for fast molecule flow and exchange (Figure **4-1.b**). This molecule

flow and exchange can be ascribed to two different mechanisms: diffusion and active pressure-driven flow.

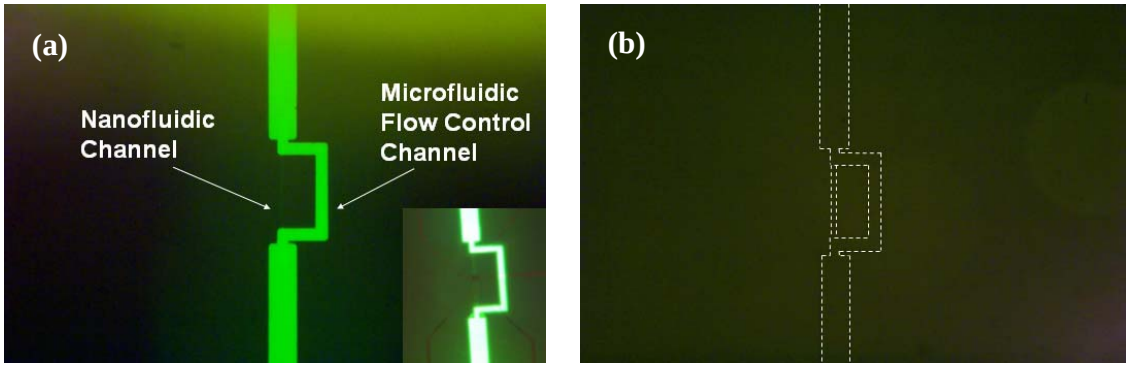

Figure **4-1**: Optical fluorescence picture of the fluidic flow control device. (a) The flow through the nanofluidic channel is controlled by using microfluidic flow control channel, (b) optical fluorescence picture of the fluidic device after DI water rinsing for 5 mins.

To differentiate between these, a study of steady-state PFC flow in the nanofluidic channel is undertaken by a focusing laser beam on the nanofluidic channel region in a version (1) device using the optical fluorescence mode of a *WITec* Raman spectroscopy system, and emission light intensity from the nanofluidic channel region is measured. Specifically, we use optical fluorescence to verify that steady-state molecule flow through the nanofluidic channel is dominantly induced by the steady-state pressure across the microfluidic flow control channel and not by diffusion.

Figure **4-2** shows the optical fluorescence spectra produced with fluorescein solution infused through the device to differentiate from potential auto-fluorescence background noise. And the result is consistent to the characteristic spectra of Alexa Fluor fluorescein molecule used.

Figure **4-3** shows the temporal fluorescence light intensity (integrated between 505 nm and 525 nm) on infusing fluorescein solution at syringe pump flow rates of 0.5 ml/hr and 1 ml/hr. As can be seen, the emission light intensity remains at constant level for both steady-state flow rates implying the molecules traverse the nanofluidic channel measuring region before photo bleaching.

Figure **4-4** shows the temporal fluorescence light intensity in the nanofluidic channel after stopping fluorescein solution infusion into the microfluidic flow control channel. The previously infused fluorescein molecules in the stagnant nanofluidic channel flow begin to bleach under the incident laser light and, therefore, the total emission light intensity decays as seen. About 25% light intensity decrease is detected within 20 minutes.

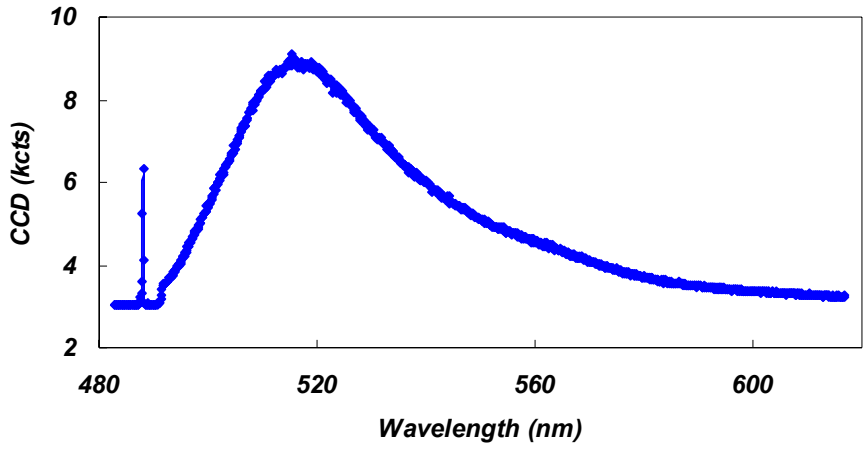

Figure **4-2**: Optical fluorescence spectra produced in the nanofluidic channel region for a version (1) device with fluorescein solution infused through the device.

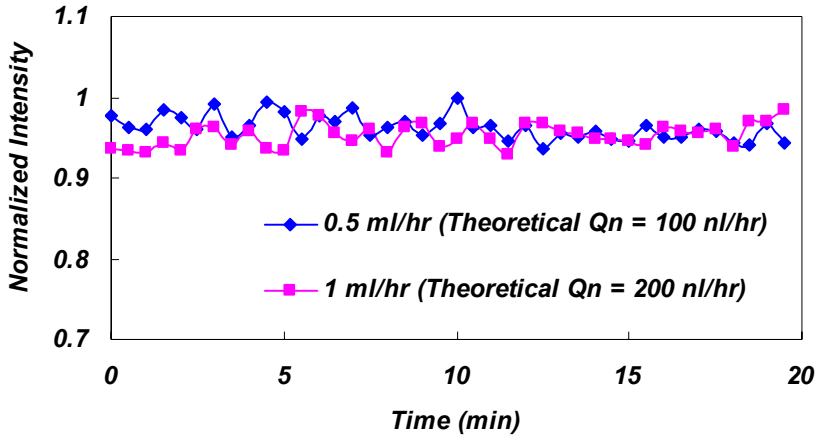

Figure **4-3**: Temporal fluorescence spectrum (integrated between 505 nm and 525 nm) behavior in the nanofluidic channel on syringe infusion of a fluorescein solution at constant rates of 0.5 ml/hr and 1 ml/hr with corresponding theoretical nanofluidic flow rate of 100 nl/hr and 200 nl/hr respectively.

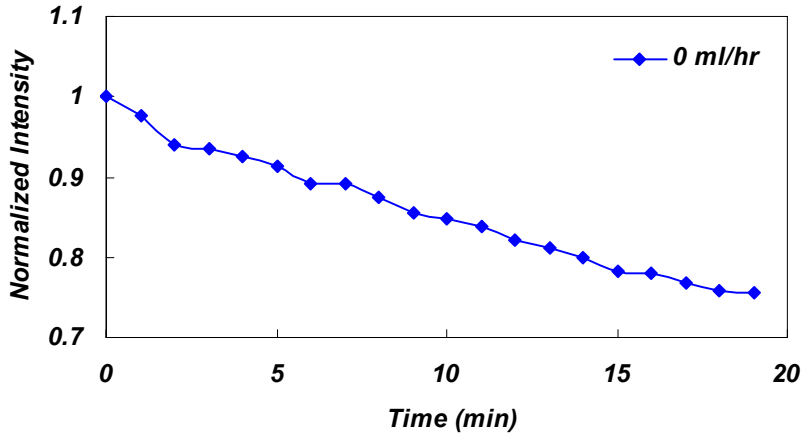

Figure **4-4**: Temporal fluorescence spectrum (integrated between 505 nm and 525 nm) behavior in the nanofluidic channel after stopping the fluorescein solution infusion. The previously infused fluorescein molecules bleach under the incident laser causing a 25% light intensity decrease within 20 minutes.

These results establish that molecular diffusion is not dominant enough to replace the bleached molecules. However, the active pressure-driven flow can transport the fluorescein molecules fast enough to overcome the photo bleaching effect and sustain the light intensity at a constant level. Since the calculated flow rate ratio Q_n/Q_m based on the designed channel dimensions is $2x10^{-4}$:1 from Eq. **2.7** for this device, and since a microfluidic channel flow rate of 0.5 ml/hr or more can stop bleaching, we deduce that a nanofluidic channel flow rate of 100 nl/hr with an average fluorescein molecule velocity of 1.74 cm/s can stop bleaching.

Another assessment of PFC nanofluidic channel flow control possibilities and steady-state flow rate is undertaken using the PFC version (2) configuration with an additional series-connected serpentine microfluidic channel (Figure **3-1.c**). The nanofluidic channel steady-state flow rate is monitored in this preliminary evaluation study by using the filling rate of the serpentine microfluidic channel. This filling rate is determined by optically tracking the position, as a function of time, of the water-air interface defining the filling front in the serpentine microfluidic channel and the designed cross-sectional area. We then assume that the filling rate of the serpentine microfluidic channel determines the steady-state flow rate of the nanofluidic channel with which it is in series. For this experiment, DI water is infused through the device at different flow rates controlled by a syringe pump (Figure **3-5.b**). The results of these measurements are labeled “experimental values” in Figure **4-5** and are plotted there against the syringe flow rate (equivalently, the microfluidic flow control channel flow rate). In Figure **4-5** we also plot what we term the “theoretical values” for the nanofluidic channel flow rate

based on the actual nanofluidic channel dimensions (Figure **3-4**) and the designed microfluidic channel geometrical dimensions. These values are determined by Eq. **2.6**, for which a computer model is used to evaluate C_n and C_m. The resulting computation gives a flow rate ratio Q_n/Q_m of 7.7x10^{-5}:1 for the device used. Since the microfluidic flow control channel (equivalently, syringe) flow rate is known, Q_n is then readily determined. As seen in Figure **4-5**, the experimental nanofluidic flow rate is about 22 times slower than the theoretical nanofluidic flow rate.

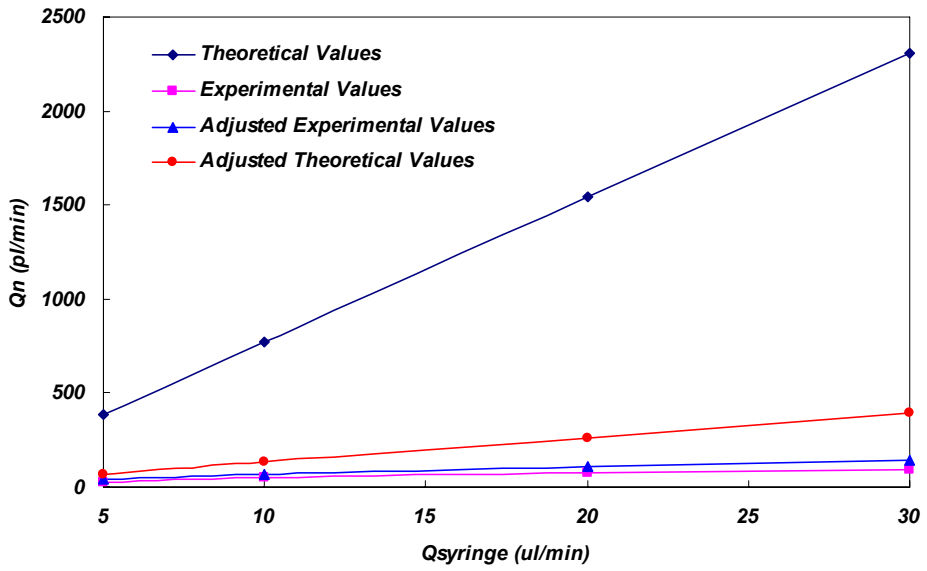

Figure **4-5**: Nanofluidic channel flow rates as a function of syringe, or equivalently, microfluidic flow control channel flow rates. Shown are the experimental values obtained by tracking flow in the serpentine microfluidic channel, the theoretical values calculated from Q_n/Q_m and the syringe flow rates, and the same curves adjusted for fabrication-caused dimension changes.

However, both of the experimental and theoretical curves are developed using designed microfluidic channel dimensions. In view of the use of wet isotropic etching for defining the microfluidic channels in the fabrication processes, and in view of the importance of both microfluidic channel cross-sectional dimensions, we investigate the final cross sections of the microfluidic flow control channel and of the serpentine microfluidic channel using FESEM (Figure **4-6**). Undercut profiles typical of wet isotropic etching are seen for both types of microfluidic channels. The actual cross-sectional dimensions are shown in this figure.

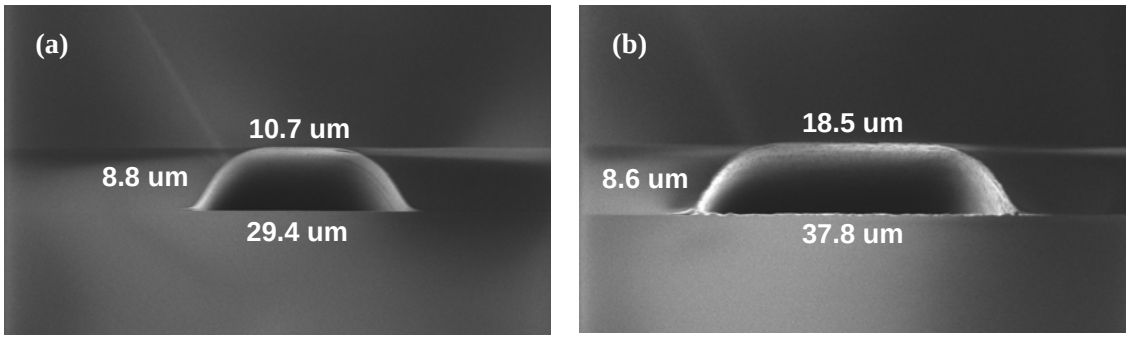

Figure **4-6**: (a) Cross-sectional FESEM picture of bonded microfluidic flow control channel, (b) cross-sectional FESEM picture of bonded serpentine microfluidic channel.

Based on the isotropic etching geometry and etching depth into the glass substrate shown in Figure **4-6.b**, the actual serpentine microfluidic channel cross-sectional area is calculated to actually be 46.6% larger than what is designed. This larger serpentine microfluidic channel width dimension resulting from isotropic wet etching implies that the actual nanofluidic channel flow is larger than that given by the experimental curve of Figure **4-5**. Using this increased cross-sectional area value leads to the “adjusted

experimental values" curve seen in Figure **4-5**. As seen, the smallest flow rate we can currently measure in our PFC device is about 1 pl/s. This is our current measurement limitation and not the smallest possible flow rate. We note that our measured flow rate is much smaller than the smallest, reported, measured nanofluidic channel flow rate of 30 pl/s [**1**].

A fabrication-caused increase in the microfluidic flow control channel cross section has a corresponding impact on the theoretical curve of Figure **4-5**. To be specific, the flow rate ratio of Q_n/Q_m which is multiplied times the syringe flow rate to get the theoretical nanofluidic channel flow rate is decreased to 1.31×10^{-5}:1 using a computational program based on the corrected etching geometry shown in Figure **4-6.a**. Using this ratio results in the "adjusted theoretical values" curve also in Figure **4-5**. As seen, the adjusted experimental flow rate is about 2 times slower than the adjusted theoretical values. These differences can arise from assumptions in the fluid dynamics modeling; e.g., the neglect of electrostatic interactions with the channel walls [**2**], and the neglect of a possibly larger viscosity coefficient for DI water in nanofluidic structures [**3**]. Inclusion of these effects will lower the calculated flow rate. The difference also can arise from our assumption, in determining the experimental curve of Figure **4-5**, that the serpentine microfluidic channel filling rate is equal to the steady-state nanofluidic channel flow rate. This neglects DI water wetting effects and evaporation effects [**1**] in the serpentine microfluidic channel. Inclusion of these effects will raise the experimental flow rate. All these multiple sources are difficult to differentiate and quantify at present. However, the plots of Figure **4-5** indicate that accounting for the correct microfluidic

channel dimensions is of primary concern in making precise nanofluidic channel flow rate measurements. Corrections due to wetting effects, interactions with the walls, and evaporation effects, which is suggested as a topic for further study in chapter 6, are bracketed by this assessment and are seen to be more subtle, at least for the case of DI water.

4.2 Conclusions

In conclusion, we present a novel PFC method for actively controlling nanofluidic flow with microfluidic flow and thereby provide a solution to the nanofluidic/external macro-fluidic system flow control/interfacing issue. The PFC approach uses a parallel connection of a microfluidic flow control channel with a nanofluidic channel. A theoretical model has been constructed and studied to reveal how the flow rate ratio between microfluidic flow and nanofluidic flow can be adjusted depending on micro- and nano-fluidic channel dimensions. We show that such a parallel approach makes it possible to have a broad range of fine flow rate control through the nanofluidic channel even with a system driven by a simple syringe pump.

Various characterization techniques are used to evaluate the resulting PFC device. These establish the active molecule flow in the nanofluidic flow control device. A novel method for actual flow monitoring measures nanofluidic flow rates in a PFC device by tracking the water-air interface filling front in a serpentine microfluidic channel connected in series. Flow rate differences between theoretical and experimental values are seen and shown to be due primarily to fabrication issues. Effects such as electrostatic

interactions with the channel walls, wetting, and evaporation effects are shown to be secondary, at least for the DI water used. These experiments have established the effectiveness and utility of our PFC configuration. We believe this novel nanofluidic flow control and characterization approach points the way to significant advances in Nano-Total Analysis Systems (nTAS) and miniaturized chemical processing systems.

References

1. K.J.A. Westin,C.H. Choi, and K.S. Breuer, "A Novel System for Measuring Liquid Flow Rates with Nanoliter per Minute Resolution," *Experiments in Fluids* **34:** 635-642, (2003)

2. F.H.J. Van Der Heyden, D. Stein, and C. Dekker, "Streaming Currents in a Single Nanofluidic Channel," *Physical Review Letters* **95:** 116104, (2005)

3. E. Tamaki, A. Hibara, H.B. Kim, M. Tokeshi, and T. Kitamori, "Pressure-driven Flow Control System for Nanofluidic Chemical Process," *Journal of Chromatography A* **1137:** 256-262, (2006)

Chapter 5

Experiment Results and Discussions

In this chapter, electrical characterization (DC and AC) of the integrated biomolecule detection system is undertaken with air or by infusing different concentrations of monobasic potassium phosphate (KH_2PO_4) solution through the system. All of the electrical measurements are taken on a micromanipulation probe station (Micromanipulator Inc.) for electrical noise shielding. An Agilent 4145 semiconductor analyzer is used for DC characterization and an Agilent 4284A LCR meter is used for AC characterization.

We also provide a demonstration of the biomolecule sensing capabilities of our devices. Probe molecules with amino groups (cysteamine (C_2H_7NS) from Sigma-Aldrich) are first self-assembled on the gold electrodes, and target nano-particles (quantum dots) with carboxyl groups (COOH) (Qdot 565 from Invitrogen Corp.) then are bonded with the probe molecules. Both of binding occurrences are detected by measuring the electrical capacitance change. Also, with the use of quantum dots, optical fluorescence mode of the *WITec* Raman spectroscopy system is again used to verify cause of the electrical signal change due to the probe and target molecule attachment. This successful electrical detection of the common amino-carboxyl binding process, substantiated by independent measurements, shows the potential detection applications of our structure for other biomolecules.

5.1 DC Measurements

DC and AC electrical measurements between the two defining electrodes of our nano-gap sensing structure are also used to probe the structure. DC measurements are taken to demonstrate that we can successfully construct our nano-gap sensing device. Figure **5-1** shows the linear I-V curve before middle sacrificial layer of metal (Ni) etching to show the conductive behavior of the patterned metal lines. As we can see, the resistance of conductive lines is about 2000 Ohms which is consistent with the theoretical value calculated from the patterned conductive line length and thickness.

Figure **5-2** shows the nonlinear I-V curve with air in the nano-gap sensing device after etching the sacrificial layer of nickel with etchant and rinsing with DI water. As we can see, the leaky resistance is larger than 5 GOhms showing the high quality of device substrate insulation.

Figure **5-3** shows the breakdown behavior (blue curve) of the device with air present, which is caused by the gold electrodes peeling off ascribed to the extremely strong electric field across the nano-gap capacitor electrodes under external voltage. The linear I-V curve of device after complete breakdown (red curve) shows the exactly same conductive line resistance with the one before sacrificial layer of metal etching. As seen in the figure, the device breaks down at about 17.5 voltages with corresponding electric field of 3.5 MV/cm.

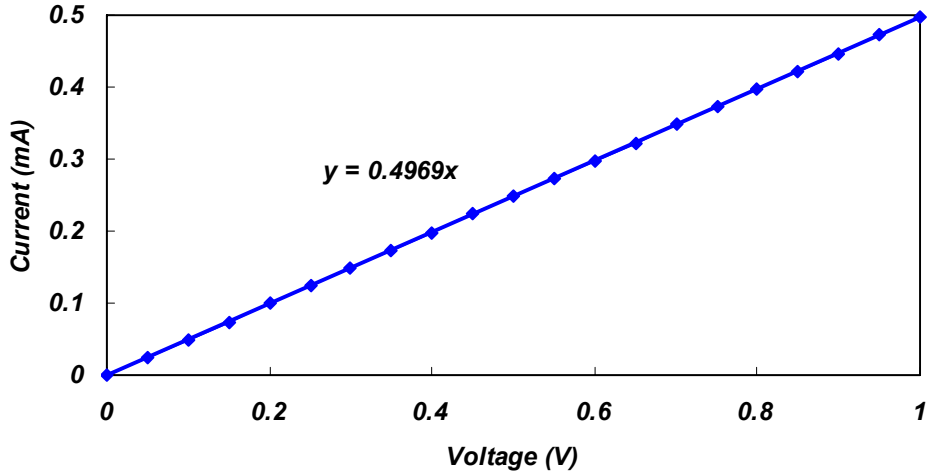

Figure **5-1**: Linear I-V curve before etching away the sacrificial layer of nickel.

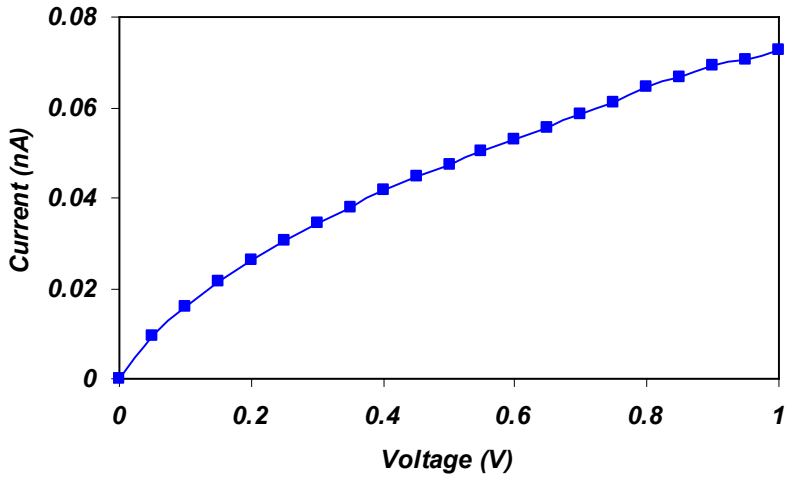

Figure **5-2**: Nonlinear I-V curve with air in the nano-gap sensing device after etching the sacrificial layer of nickel.

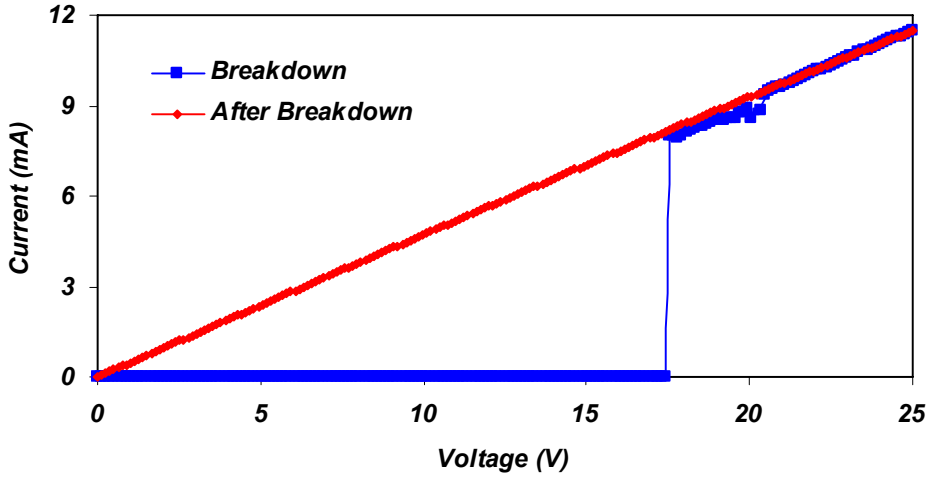

Figure **5-3**: I-V curve of breakdown and post breakdown with air in the nano-gap sensing device.

5.2 AC Measurements

AC electrical characterization is first taken in the frequency range from 1 KHz to 1 MHz. Data from such measurements are shown in Figure **5-4** for the case of infusing different concentrations of KH_2PO_4 solution. A geometric capacitance calculated from the designed nano-gap capacitor dimensions including distance (50 nm) and area (40 μm^2) is also shown. As we can see, the capacitance value increases with the solution concentration. This is due to the smaller characteristic thickness of diffuse layer of more concentrated electrolyte solution which is depicted in the theoretical analysis in Chapter 2. Also, the capacitance decreases with frequency because of the response regimes of the various dielectric mechanisms as shown in Figure **5-5**. As the frequency increases, the

slower mechanisms drop out, leaving the faster ones to contribute to the storage ($\varepsilon_r^{'}$) which is the real part of permittivity and the loss factor ($\varepsilon_r^{''}$) which is the imaginary part. This makes the measured capacitance tends to the geometric capacitance value. Most significantly, the results show the same order of capacitance values in spite of orders of concentration change. This can be ascribed to the effects of diffuse layer overlapping, which causes the diffuse layer capacitance increase dramatically. Therefore, the total capacitance is dominated by the capacitance component due to the Helmholtz layer, which is in the same order for different concentrations of electrolyte solution.

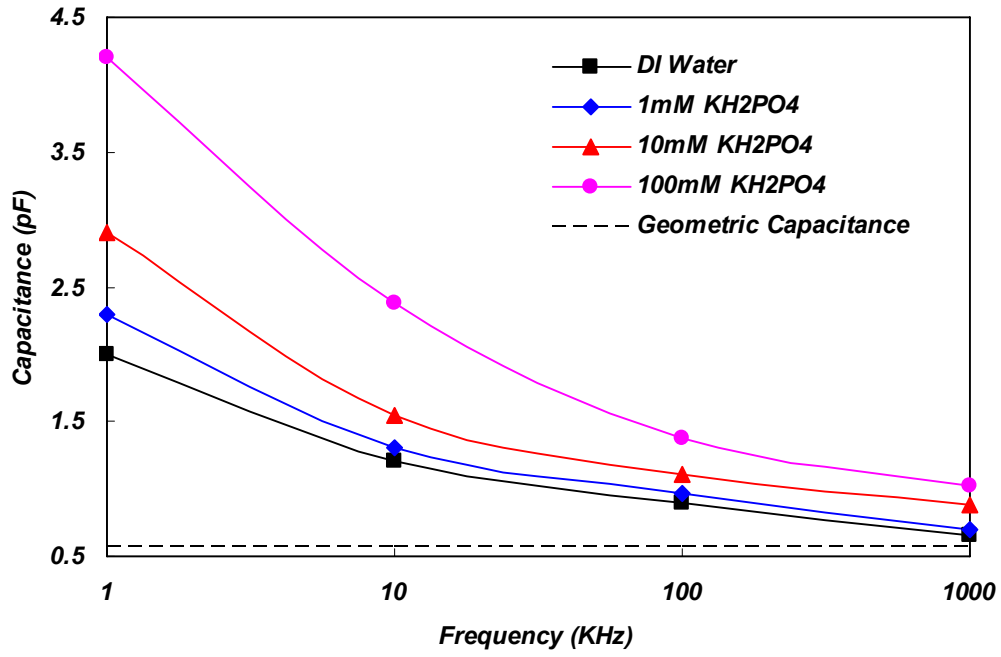

Figure **5-4**: AC electrical characterization of nano-gap sensing device with different concentrations of KH_2PO_4 solution. Geometric capacitance is calculated based on designed nano-gap sensing device dimensions.

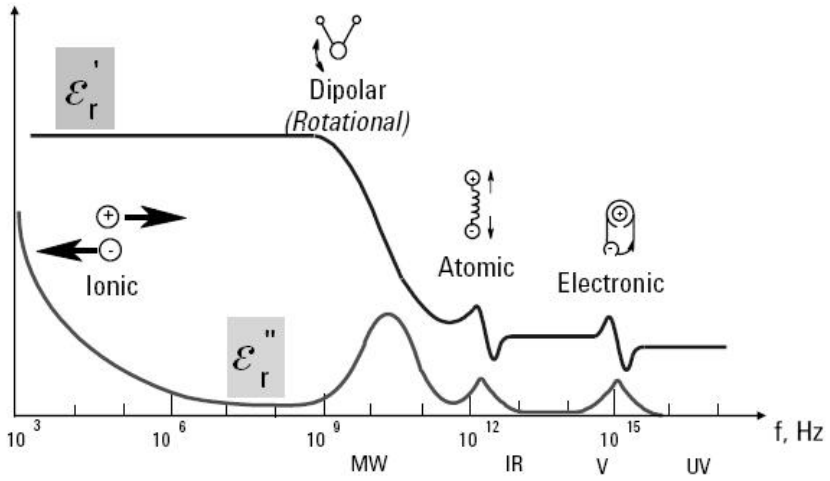

Figure **5-5**: Frequency response of dielectric mechanisms [**1**].

We also successfully self-assemble molecules on the nano-gap gold electrodes and subsequently demonstrate the biomolecule sensing capabilities of our devices. To accomplish this, probe molecules with amino groups are first self-assembled on the gold electrodes by infusing a 20 mM cysteamine aqueous solution (90% IPA and 10% DI water) for 4 hours, and then target nano-particles (quantum dots) with carboxyl groups (Qdot 565 from Invitrogen Corp.) are bonded with the probe molecules by infusing a 80 nM Qdot 565 solution in 50 mM KH_2PO_4 solution for 4 hours. Both of binding occurrences are detected by measuring the electrical capacitance change in the frequency range from 10 kHz to 1 MHz (Figure **5-6**) after changing to infuse DI water as the measurement medium for 1 hour. As we can see, cysteamine attachment decreases the capacitance which is due to its smaller dielectric constant compared with DI water and the pushing effect of the electrical double layers further from the electrodes. The quantum dot attachment further decreases the capacitance due to the same mechanisms. About a

15% capacitance change with the amino-carboxyl binding occurrence is detected at 1 MHz.

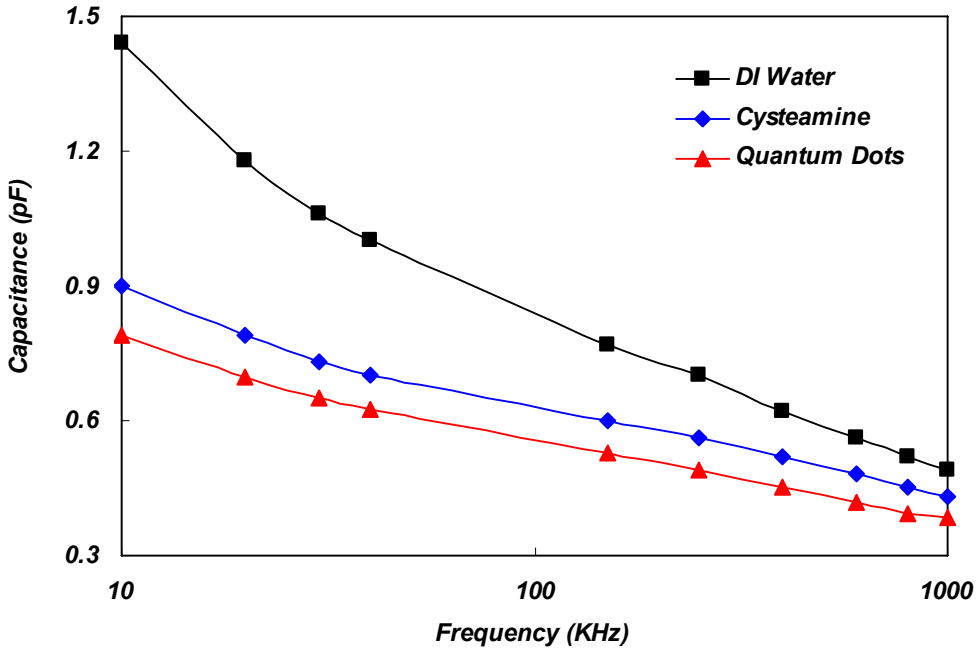

Figure **5-6**: AC electrical characterization of the nano-gap sensing device demonstrating biomolecule sensing capabilities.

5.3 Optical Fluorescence Characterization of Biomolecule Assembling

To verify that the quantum dots used in previous demonstration actually do attach, we again employ the optical fluorescence mode of the *WITec* Raman spectroscopy system using a 488 nm blue laser source. For these fluorescence measurements the bonded PDMS is peeled off, and any solution left is dried after probe and target molecules attaching and rinsing by DI water, and an optical objective is brought close to

the embedded electrodes. Figure **5-7** shows the fluorescence spectrum verification of cysteamine molecule self assembling and quantum dot binding.

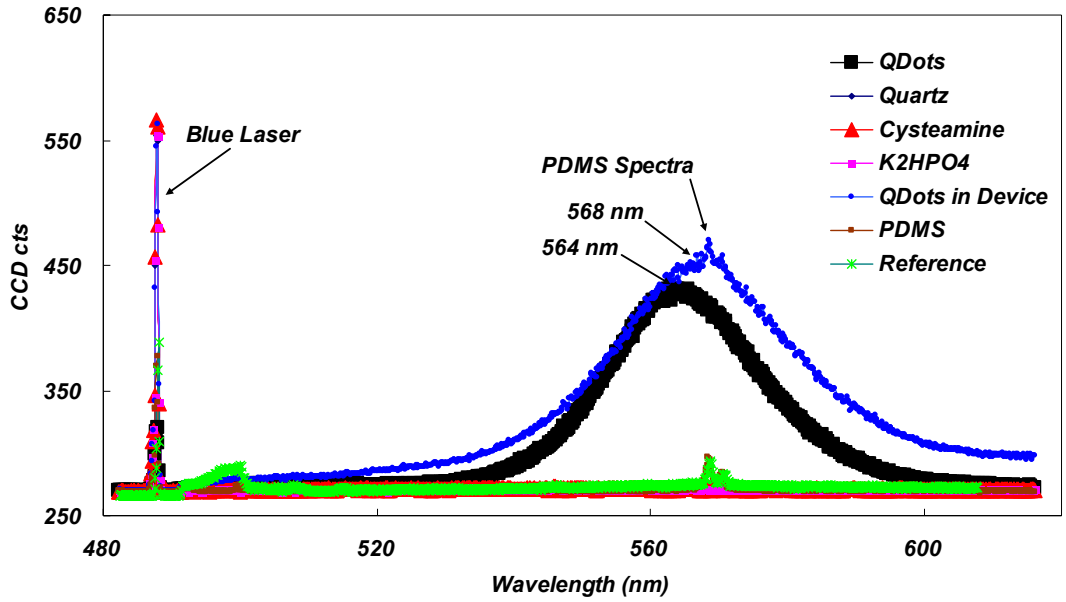

Figure **5-7**: Optical fluorescence spectrum obtained under different conditions. The fluorescence spectra of a device with quantum dots attached (blue curve with peak of 568 nm) is consistent with a control solution of quantum dots (black curve with peak of 564 nm), which verifies quantum dots are actually attached on the electrode surfaces in the nanofluidic channel. The shift between these two spectra is due to aggregation of the attached quantum dots.

As seen in Figure **5-7**, the fluorescence spectrum of a device with quantum dots attached (blue) is consistent with a control solution of quantum dots (black), which verifies quantum dots are actually attached on the electrode surface in the nanofluidic channel. The shift between these two spectra is due to aggregation of the attached quantum dots which will be verified in following experiment. To ensure the attached and control spectra are truly attributable to the quantum dots, spectra of other materials

involved in the devices and demonstrations are also shown in the figure. As seen, these show no corresponding peak. It can be noted that there is a small peak on the top of the device spectra. This is due to the PDMS residue as may be seen by comparing with the PDMS fluorescence spectra.

To verify the shift between blue and black spectra is due to aggregation of the attached quantum dots in Figure **5-7**, a control experiment is carried out by taking the fluorescence spectrum with a quantum dot solution before and after the solution is dried out (Figure **5-8**). As seen, when the solution dries out, the quantum dots begin to aggregate together, and the resulting larger size of aggregated quantum dots causes the red shift of the characteristic spectrum.

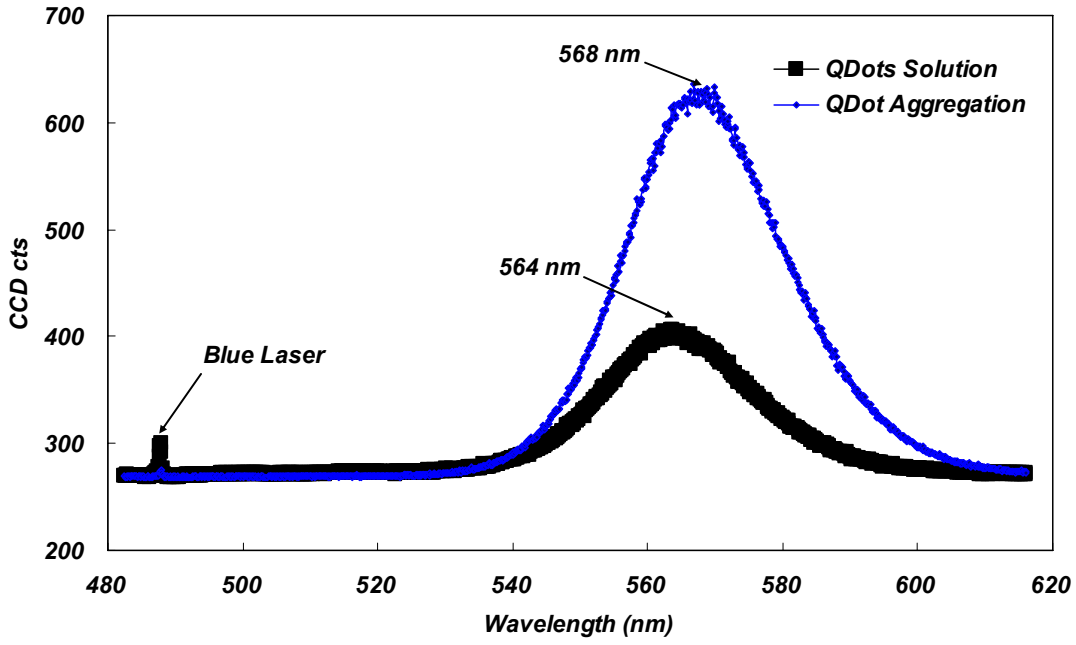

Figure **5-8**: Optical fluorescence spectrum of control experiment. The quantum dot aggregation due to solution drying out causes the spectrum red shift.

5.4 Conclusions

In this experiment, we construct and evaluate a self-contained nano-gap biomolecule capacitance sensor system integrated with nanofluidic flow control components. The molecule detection capability is based on the electrical capacitance change upon probe and target molecule binding on the gold electrode surfaces (spaced 50 nm) in the nano-gap sensing structure. A result of our nano-gap capacitor sensing structure design is our being able to reduce background noise from the electrical double layer, therefore, increase the system sensitivity.

AC electrical characterization is undertaken by infusing different concentrations of KH_2PO_4 solution through the integrated sensor system. Measured results show the same order of capacitance values within specific measurement frequency range from 1 kHz to 1 MHz. Therefore, it illustrates the noise shielding capabilities due to the diffuse layer overlapping.

We also provide a demonstration of biomolecule sensing capabilities of the integrated sensor system. Probe molecules (cysteamine) are first self-assembled on the electrode surfaces, and target molecules (quantum dots) then are bonded with the probe molecules. Both of binding occurrences are detected by measuring the capacitance change. About a 15% capacitance change with the amino-carboxyl binding is measured at 1 MHz. Optical fluorescence spectra are also obtained to verify that the quantum dots used in this demonstration actually do attach and cause the corresponding capacitance signal change. This successful electrical detection of the common amino-carboxyl

binding process shows the potential detection applications of our system for other biomolecules.

References

1. “Basics of Measuring the Dielectric Properties of Materials,” *Application Note 1217-1* Hewlett-Packard LTD. (1992)

Chapter 6

Summary and Future Work

6.1 Summary

In this dissertation, we introduce a self-contained nano-gap biomolecule capacitance sensor system integrated with nanofluidic flow control. This is the first time it has been accomplished, to our knowledge. The complete analytical system is based on a full analysis, design and fabrication approach, which addresses noise, sensitivity, and integration issues. This device is composed of a microfluidic flow control channel in PDMS and a nanofluidic channel in silicon oxide feeding a nano-gap capacitor sensing structure with gold electrodes. Our integrated analytical system is also capable of selectivity. This can be realized by the immobilization of specific probe and target molecules on the electrode surfaces.

The fundamental biomolecule detection capability is based on the electrical capacitance change upon probe and target molecule binding on the gold electrode surfaces in the nano-gap sensing structure. A theoretical analysis of the electrical double layer configuration between the nano-gap electrodes is presented based on conventional electrostatics and thermodynamics. The result shows that we are able to shield unwanted electrochemical noise from the electrical double layers by using the sub-50 nm gap sensing structure to overlap the electrical double layers. The overlapping results in the

capacitance from the diffuse layers to increase dramatically, therefore, enhance system sensitivity to capacitance component due to probe and target molecule binding.

The successful nanofluidic flow control through the nano-gap sensing structure for active molecule flow and exchange is accomplished by using a novel nanofluidic parallel flow control (PFC) component, which is initially developed using a theoretical analysis to support its feasibility. The PFC approach uses a parallel connection of a microfluidic flow control channel and a nanofluidic channel. A theoretical model has been constructed and studied to reveal how the flow rate ratio between nanofluidic flow and microfluidic flow can be adjusted depending on nano- and micro-fluidic channel dimensions. We show that such a parallel approach makes it possible to have a broad range of fine flow rate control through the nanofluidic channel even with a system driven by a simple syringe pump. This configuration also facilitates the interfacing between nanofluidic systems and external macro fluidic systems.

To demonstrate the feasibility of parallel flow control approach to be utilized in our biomolecule detection system, we construct individual nanofluidic flow control devices based on glass etching and bonding (version (1) and version (2)). Various characterization techniques are used to evaluate the resulting PFC device. These establish the active molecule flow in the nanofluidic flow control device. Furthermore, a novel method for actual flow monitoring measure the nanofluidic flow rates in a PFC device by tracking the water-air interface filling front in a series-connected serpentine microfluidic channel. Nanofluidic channel flow rates as low as 1 pl/s are measured exceeding the current lowest limit of 30 pl/s reported in literature [**1**].

We also fabricate the integrated analytical system and provide a demonstration of the biomolecule sensing capabilities of our integrated system. Probe molecules with amino groups (cysteamine (C_2H_7NS) from Sigma-Aldrich) are first self-assembled on the gold electrodes, and target nano-particles (quantum dots) with carboxyl groups (COOH) (Qdot 565 from Invitrogen Corp.) then are bonded with the probe molecules. Both of binding occurrences are detected by measuring the electrical capacitance change. We are able to detect about 15% capacitance changes with this amino-carboxyl binding occurrence at 1 MHz. Also, with the use of quantum dots, optical fluorescence mode of a *WITec* Raman spectroscopy system is used to verify cause of the electrical signal change due to the probe and target molecule attachment. This successful electrical detection of the common amino-carboxyl binding process, substantiated by independent measurements, shows the potential detection applications of our structure for other biomolecules.

6.2 Future Work

In this dissertation, the self-contained nano-gap biomolecule capacitance sensor system integrated with nanofluidic control is constructed. The system application in biomolecule detection is demonstrated by measuring the electrical capacitance change. The fundamental principles behind the system are presented in detail. Corresponding theoretical analysis and experimental investigation are undertaken to support the whole system design. There are still some challenges to be overcome to allow the attainment of better performance in future work.

6.2.1 Fabrication Processes

The electrode surfaces in the nano-gap capacitor structure require high surface quality to optimize the biomolecule assembling. High temperature annealing may improve the gold surfaces after the first layer of metal evaporation. It may improve the surface assembling density of the biomolecules, and, therefore, the sensitivity of the system can be improved.

On the other hand, the step of a 10 μm thick ECR-PECVD oxide deposition is extremely time-consuming and also unsuitable for commercial production. The dielectric and mechanical properties produced by this deposition are, in general, lacking. Furthermore, given the high aspect ratio of nanofluidic channel width to height, and the thin capping layer used, the mechanical deformation of the capping layer can be serious barriers to obtaining stable analytical systems with acceptable performance. To improve this, mechanical polishing and bonding technology can be utilized. Instead of depositing 10 μm thick oxide on the top, only 2 μm thick silicon oxide is required. After polishing, a blank glass slide can be bonded with the device to improve the mechanical stability and achieve better dielectric properties.

6.2.2 Impedance Spectroscopy

The theoretical analysis based on a simplified circuit model in this work mainly focuses on different capacitance components and relevant effects in our electrochemical sensor system. This simplified model is not capable to characterize the complete

electrochemical system comprehensively by neglecting the internal complexities. Moreover, capacitance data are only acquired within certain frequency range due to the limited functionality of Agilent 4284A LCR meter used. Therefore, more advanced data analysis and equivalent circuit model simulation can be undertaken with an impedance spectroscopy over broader frequency range, subsequently, to better characterize this electrochemical system physically and chemically. Furthermore, with sufficient data over broader frequency range, Kramers-Kronig analysis can also be applied to evaluate the data quality, and therefore, evaluate the complete electrochemical system in term of linearity, causal relation, and stability.

6.2.3 Device Robustness

Due to the nano-gap scale of the sensing structure and surrounding dielectric materials, a small amount of accumulated charge on the electrodes can produce an extremely strong electric field between the two opposite electrodes. Because of this, the nano-gap sensing device turns out to be very easily broken down electrostatically. A better packaging method needs to be proposed to prevent the electrostatic break down. Use of other electrode materials such as semiconductor materials with stronger adhesion strength with substrate may be another potential way to improve the device robustness. Other than that, configuration of vertical electrode setup instead of current horizontal layer structure can be used to improve device robustness.

6.2.4 Electrode Materials

Silicon-based ISFET biomolecular sensors have shown the flexibility and versatility of silicon in the sensing field. With the high sensitivity to surface charge density, semiconductors can be used as the electrode materials instead of metals to improve the system sensitivity. Semiconductor material use may also contribute to improving device robustness.

6.2.5 Sensitivity

Signal amplification method can be applied in this system by using nano-particles capped with target molecules and corresponding interactant molecule pairings (e.g., double strand DNA) to improve the sensitivity [**2**]. The amplification principle is based on the extremely large number of corresponding interactant molecule pairings which can be more easily detected for each target molecule binding event.

6.2.6 Application

The future goal of this integrated analytical system lies in its being able to be applied in detecting actual biomolecules of interest especially for practical clinical diagnosis. One of the potential applications can be its use to detect cancer formation. Recent research has shown that methylated DNA is one possible screening marker for cancer [**3**]. Therefore, by using the affinitive MBD protein (Methyl-CpG Binding

Domain) which is able to distinguish and bind methylated DNA, methylated DNA related with specific cancer could be detected in our system.

References

1. K.J.A. Westin,C.H. Choi, and K.S. Breuer, "A Novel System for Measuring Liquid Flow Rates with Nanoliter per Minute Resolution," *Experiments in Fluids* **34:** 635-642, (2003)

2. J.M. Nam, C.S. Thaxton, and C.A. Mirkin, "Nanoparticle-based Bio-bar Codes for the Ultrasensitive Detection of Proteins," *Science* **301:** 1884-1886, (2003)

3. M.F. Fraga, E. Ballestar, G. Montoya, P. Taysavang, P.A. Wade, and M. Esteller, "The Affinity of Different MBD Proteins for a Specific Methylated Locus Depends on Their Intrinsic Binding Properties," *Nucleic Acids Research* **31:** 1765-1774, (2003)

Appendix

Nontechnical Abstract

Since the 1940s when Leland C. Clark fist measured glucose concentration with the famous Clark oxygen electrode, biomolecular sensors have played a significant role in human healthcare. The fundamental of biomolecular sensors relies on molecular interactant pairings (visualized as lock-key pairings) in biological organisms based on structural affinity, such as enzyme-substrate, enzyme-coenzyme, antigen-antibody, biotin-streptavidin, and widely known double strand DNA, etc. In such couplings, one component (e.g., lock) can be fixed and used as the probe, and hence can be used to catch and detect the other component (e.g., key) which is identified as the target. Consequently, biomolecular sensors can realize high selectivity and sensitivity which is required in detecting a variety of biomolecules.

Further, with the continuous development of novel materials, principles and technologies, especially the emergence of Micro-Electro-Mechanical Systems (MEMS) technology (1970s) and biochip technology (1990s), current biomolecular sensors often comprise Micro-Total Analysis Systems (μTAS) with minimization, integration, and intelligence. Portable medical diagnostic instruments, aimed to offer point of care testing (POCT) in a timely manner, have been pioneered by the glucose meters commercially developed in 1993. The ultimate goal scientists have been striving for is to realize a Lab-on-a-Chip system which integrates analyte sample flow control, biomolecule

detection, and processing on a single chip. These essentially necessitate a suitable sensing approach for highly integrated analytical systems.

In this work, we construct a self-contained nano-gap biomolecule capacitance sensor system with nanofluidic control. This work represents the first time such a device has been developed, to our knowledge. It is based on a full analysis, design and fabrication approach, which addresses noise, sensitivity, and integration issues. This sensor system consists of an integrated microfluidic channel in PDMS and a nanofluidic channel in silicon oxide, feeding a nano-gap capacitor sensing structure with gold electrodes. The molecule detection capability is based on the electrical capacitance change upon probe and target molecule binding on the gold electrode surfaces (spaced 50 nm) in the nano-gap sensing structure. A schematic model and corresponding theoretical analysis are performed to show the noise shielding advantages in our specific nano-gap sensing structures ascribed to the electrical double layer overlapping within 50 nm gap capacitor structure.

The active molecule flow and exchange through the nano-gap sensing structure is fundamentally required for implementing a rapidly responsive biomolecular sensor system. These issues are solved using a microfluidic flow control channel connected with the nanofluidic channel in parallel, initially developed using a theoretical analysis to support its feasibility. By using this unique parallel connection configuration, an extremely fine controlled flow rate through the nanofluidic channel leading to and from the nano-gap sensing structure is realized and the interfacing problems with the external macro-fluidic world are solved successfully.

Biomolecule sensing capabilities of our sensor systems are also demonstrated in this work by self-assembling probe molecules (cysteamine with amino groups) and attaching target molecules (quantum dots with carboxyl groups) on the gold electrode surfaces. Electrical capacitance signals are measured while infusing DI water through the system following both of binding occurrences. About 15% capacitance changes following this amino-carboxyl binding occurrence are detected. Optical fluorescence spectra are also acquired to verify that the quantum dots used in this demonstration do attach and cause the corresponding capacitance changes. This successful electrical detection of the common amino-carboxyl binding process shows the potential detection applications of our systems for other biomolecules.

VITA

Huinan Liang

EDUCATION

Ph.D., Engineering Science and Mechanics, 12/2008 The Pennsylvania State University
Dissertation: A Self-contained, Nano-gap Biomolecule Capacitance Sensor System with Nanofluidic Control

M.S., Bioengineering, 05/2004 The Pennsylvania State University
Thesis: Fluorescence Based Assays in a Programmable Microfluidic Cytometer

B.S., Biomedical Engineering, 06/2002 Zhejiang University, China

RESEARCH EXPERIENCE

Research Assistant in Nanofab Facility at Penn State, Penn State University, 08/2004 -12/2008

- Developed novel approaches to construct nano-gap biomolecular sensor with nanofluidic control.
- Designed process flow and fabricated nano-gap sensing structure, established theoretical principles of noise shielding ascribed to the unique nano-gap structure, and carried out processes in nanofab.
- Invented and fabricated novel nanofluidic parallel flow control structure for nano-gap sensing structure.
- Integrated both structures, characterized and analyzed integrated sensor performance in biomolecule detection.

Research Assistant in BioMEMs Lab, Dept. of Bioengineering, Penn State University, 08/2002 - 05/2004

- Developed microdevices for microdialysis and membrane separation, established microdialysis principles, and characterized fluorescence molecule separation through membranes.
- Developed fluorescence based assays in a microfluidic cytometer, investigated hydrodynamic focusing flow, and constructed an optical sensing system with digital data acquisition/processing for cell monitoring.

Research Assistant in Biosensor National Special Lab, Zhejiang University, China, 09/2000 - 06/2002

- Developed optical chemical microarray sensors based on MEMS.